Chemical vapor deposition of graphene:

a route to device integration

Chemical vapor deposition of graphene:
a route to device integration

Proefschrift

ter verkrijging van de graad van doctor
aan de Technische Universiteit Delft,
op gezag van de Rector Magnificus prof. ir. K. C. A. M. Luyben,
voorzitter van het College voor Promoties,
in het openbaar te verdedigen
op dinsdag 3 March 2015 om 12:30 uur

door

Shou-En Zhu
Master of Materials Science and Engineering
Jilin University, China
Geboren te Fujian, China

Dit proefschrift is goedgekeurd door de promotor:
Prof. dr. G.C.A.M. Janssen

Samenstelling promotiecommissie:

Rector Magnificus	voorzitter
Prof. dr. G. C. A. M. Janssen	Technische Universiteit Delft, promotor
Prof. dr. D. J. Gravesteijn	Universiteit Twente
Prof. dr. P. G. Steeneken	Technische Universiteit Delft
	NXP semiconductors
Prof. dr. J. Schmitz	Universiteit Twente
Prof. dr. ir. R. Dekker	Technische Universiteit Delft
	Philips Research
Prof. dr. H.W. Zandbergen	Technische Universiteit Delft
Dr. ir. M. H. F. Sluiter	Technische Universiteit Delft

Printed by: Ipskamp Drukkers BV
ISBN 978-94-6186-438-3

This book is printed on FSC-certified, 100% recycled paper.

Author email: zhushouen@gmail.com

Contents

Chapter 1. Introduction.. 1
Chapter 2. Graphene synthesis by chemical vapor deposition 7
    2.1 Introduction 7
    2.2 Chemical vapor deposition 8
    2.3 CVD furnace 9
    2.4 Graphene growth... 11
Chapter 3. Molecular dynamics simulation of graphene on Cu 13
    3.1 Introduction.. 14
    3.2 Computational details 15
    3.2.1 COMB3 description of the graphene/Cu system.......................... 17
    3.2.2 High temperature simulations... 21
    3.2.3 Room temperature wrinkle formation... 23
    3.3 Summary... 30
    3.4 Acknowledgements 32
Chapter 4. Ballistic transport in CVD graphene................................. 33
    4.1 Introduction 34
    4.2 Graphene growth results 34
    4.3 Graphene transfer... 36
    4.4 Quantum transport measurement 38
    4.5 Conclusion... 42
    4.6 Acknowledgement 42
Chapter 5. Optical transmittance of multilayer graphene................... 45
    5.1 Introduction 46
    5.2 Numerical simulation.. 47
    5.3 Experimental section 49
    5.4 Conclusion... 53

5.5 Acknowledgement 53

Chapter 6. Graphene based piezoresistive pressure sensor 55

6.1 Introduction 56

6.2 Strain and displacement of pressure sensor........ 56

6.3 Resistance of graphene and Wheatstone bridge........ 59

6.4 Piezoresistivity of graphene........ 60

6.5 Conclusion........ 61

6.6 Acknowledgement 62

Chapter 7. Infrared nano-imaging of plasmons in graphene 63

7.1 Introduction........ 64

7.2 Near field optical measurement........ 65

7.3 Plasmon damping rate........ 68

7.4 Plasmon edge mode and wavelength 69

7.5 Conclusion 73

7.6 Acknowledgement........ 73

Chapter 8. Summary........ 75

8.1 Introduction 75

8.2 What does this thesis contribute to the development of a graphene technology........ 76

Bibliography........ 79

Samenvatting 89

Curriculum Vitae........ 93

List of Publications........ 95

Acknowledgement........ 97

CHAPTER 1

Introduction

Graphene is one atomic layer of graphite. It contains only one single element: carbon. Graphene has lots of special properties. It is the thinnest imaginable material, it is the strongest material ever measured (theoretical limit), it is the stiffest known material (stiffer than diamond), it is the most stretchable crystal (up to 20% elastically), it has record thermal conductivity (outperforming diamond), it can withstand the highest current density at room temperature (a million times higher than that in copper), it has the highest intrinsic mobility (100 times higher than in silicon), it conducts electricity even while the density of charge carriers approaches zero, it has the lightest charge carriers (zero rest mass), it has the longest mean free path at room temperature (micron range), it is the most impermeable (even He atoms cannot squeeze through)…

In 2010, the Nobel Prize in Physics was awarded jointly to Andre Geim and Konstantin Novoselov "*for groundbreaking experiments regarding the two-dimensional material graphene*" [1, 2]. They demonstrated the electric field effect in atomically thin carbon films for the first time in 2004 [3]. The graphene films were prepared by mechanical exfoliation (repeated peeling) of graphite with adhesive tape as shown in Fig. 1.1a. There will be plenty of graphite debris with all sorts of shapes and number of layers on the tape. With this method, it is possible to achieve monolayer graphene with flakes of 10 μm in size. The very first hand-made device by Novoselov is shown in Fig. 1.1b. By changing the gate voltage, the charge carriers can be switched between electrons and holes. This behavior resembles the ambipolar field effect in semiconductors, but there is no zero conductance region because graphene doesn't have a band gap. The device structure is also similar to the first transistor made at Bell Lab in 1947 as shown in Fig. 1.1c. In acknowledgement of this accomplishment, William Shockley, John Bardeen, and Walter Brattain were jointly awarded the 1956 Nobel Prize in Physics "*for their researches on semiconductors and their discovery of the transistor effect*" [4].

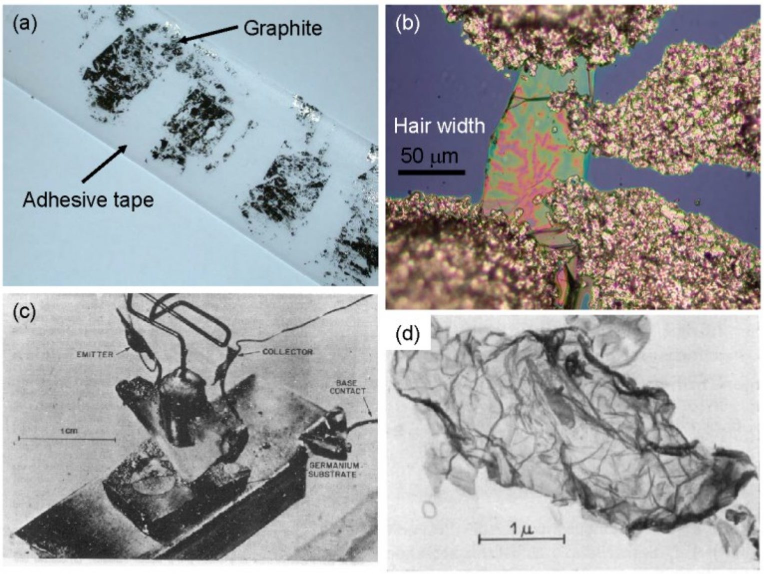

Figure 1.1: (a) Graphite debris on adhesive tape. (b) Hand-made graphene transistor, where silver paint was glued to graphene as electrode with a toothpick. [1] (c) The first point-contact transistor, where two gold point contacts were applied to a crystal of germanium (AT&T's Bell Labs) (d) Graphene produced by reduction of graphite oxide in 1962 [5].

In fact, graphene has been produced much earlier. In 1948, G. Ruess and F. Vogt observed creased flakes of graphene-oxide down to a few nm on a transmission electron microscopy (TEM) grid [6]. 14 years later, Hanns-Peter Boehm and Ulrich Hofmann produced graphene fragments by reduction of graphite oxide and identified some of them as monolayer as shown in Fig. 1.1d [5].

Thanks to the mechanical exfoliation method and first graphene transistor demonstrated by Geim and Novoselov at the University of

Manchester, graphene became experimentally accessible to researchers all over the world. It is one of the most active areas in research fields right now, and the research progress in graphene is rapidly growing. The number of scientific publications containing “graphene” in their title increases drastically every year from 2004 as shown in Fig. 1.2.

Graphene is a miracle material and provides an ideal platform for researchers to study interesting properties. The carbon-atoms are arranged in hexagonal lattices that resemble the honeycomb as shown in Fig. 1.3a and b. The carbon-carbon atoms form in-plane sp^2 covalent bonds with length of 0.142 nm, and the effective thickness of graphene is 0.335 nm [7, 8]. The Young's modulus of graphene was reported to be 1.0 ± 0.1 TPa, and failure stress is up to 130 GPa with strain up to 25% [9], which makes graphene not only the strongest material in the world but at the same time highly flexible and stretchable.

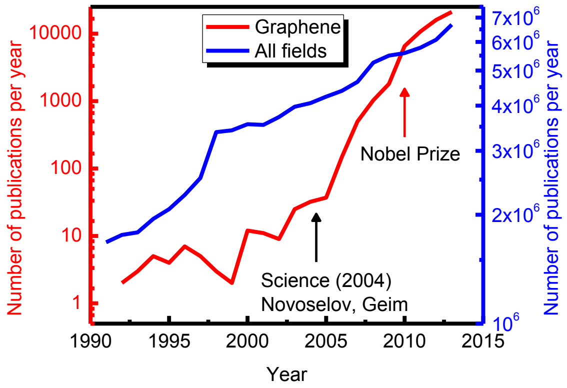

Figure 1.2: Number of Scientific publications per year and those containing “graphene” in their title. (Data acquired from Web of science, Thomson Reuters, Aug. 2014).

Graphene consists of two atoms denoted as A and B per unit cell (Fig. 1.3c). The out-of-plane p_z orbitals of carbon atoms in graphene hybridize to form lower π (valence band) and upper π^* (conduction band) bands touching at two points (K and K') in the Brillouin zone as shown in Fig. 1.3d [10]. The unique band structure makes graphene a zero-gap semimetal, and the quasiparticles in graphene exhibit a linear dispersion relation near the crossing Dirac points. The Fermi–Dirac velocity in graphene is only about 300 times less than the speed of light, which allow relativistic effects to be observed [11, 12]. The intrinsic carrier mobility of graphene was found to be ~200,000 cm^2/Vs, which is more than 100 times higher than that of silicon [13, 14]. Table 1.1 illustrates some of the important physical properties of graphene.

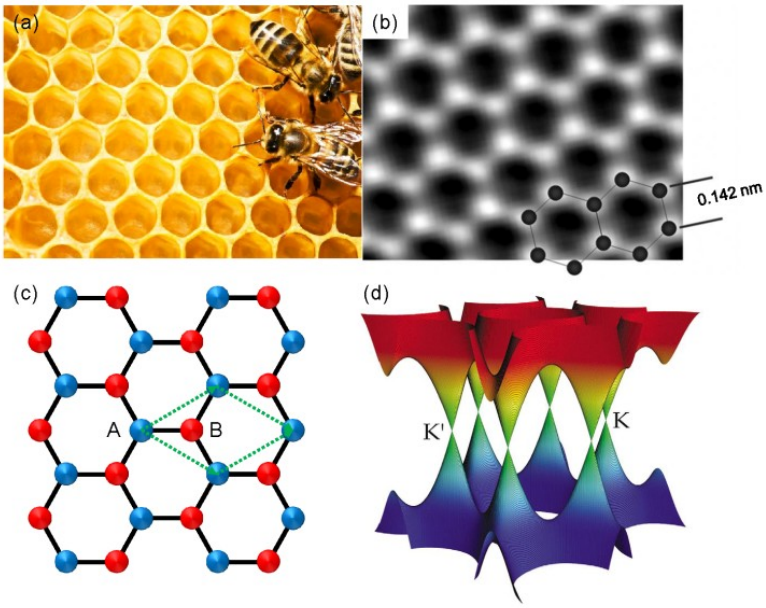

Figure 1.3: (a) Hexagonal wax cells of a honeycomb built by honey bees. (b) An atomic-resolution image of graphene sheet [23]. (c) Graphene lattice and the unite cell indicated by green dashed line. (d) Band structure of graphene. The conductance band touches the valence band at the K and K' points[11].

There are lots more of intriguing properties of graphene, and diverse applications can potentially be realized with this material as shown in Fig. 1.4. The European Commission has appointed the Graphene Flagship as one of Europe's first ten-year FET flagships with a budget of one billion euros, aiming to bring this material from academic laboratories into society in ten years. [15]

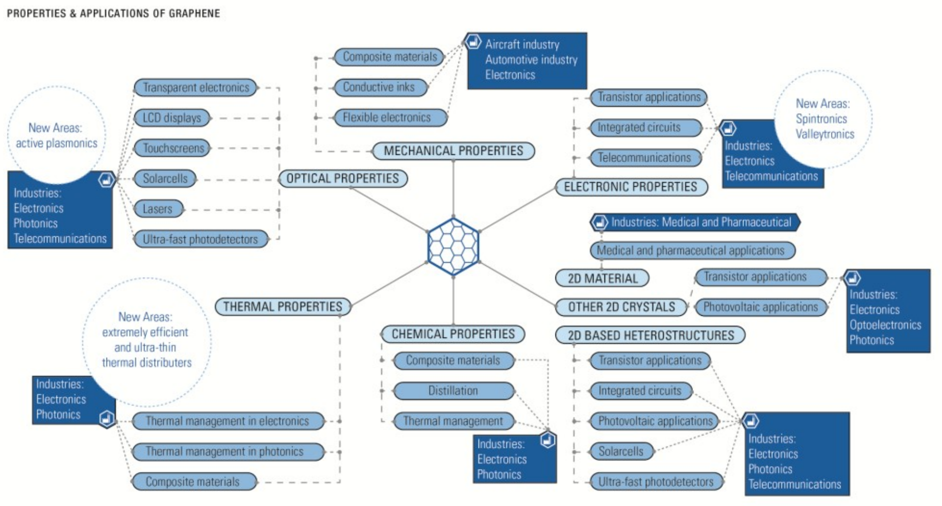

Figure 1.4 Properties and applications of graphene. (Image Courtesy of Graphene Flagship)

Table 1.1: Typical properties of graphene.

Typical properties of graphene			
Properties	**Value**	**Unit**	**Refs.**
Thickness	0.335	nm	[7, 8]
Surface area	2,630	m^2/g	[16]
Thermal expansion coefficient	$(-8.0 \pm 0.7) \times 10^{-6}$ (RT)	K^{-1}	[17]
Young's modulus	1.0 ± 0.1	TPa	[9]
Fracture strain	25	%	[9]
Melting temperature	~4900	K	[18]
Thermal conductivity	~5000	W/mK	[19]
Optical transmittance	97.4 (550 nm) 97.7 (650 nm)	%	[20, 21]
Intrinsic carrier mobility	200,000	cm^2/Vs	[14, 22]

Although enormous amount of efforts have been devoted into graphene research, there is still a large gap between academia and industry. How to cross the valley of death from research to business is still an open question. There are several remaining challenges for graphene that in my mind need to be overcome before it can generate an high impact for our society: 1. Is it possible to launch useful and simple industrial products which can be used already now? 2. Do we have a method to mass produce large-scale and high-quality graphene in low cost? 3. Can we standardize the properties of graphene? 4. What is the most promising future application for graphene?

In this thesis, I will report a potential mass production method and a few promising applications for large-scale graphene films. In chapter 2, I will mainly focus on the growth of graphene. In chapter 3, I will discuss about the interaction between graphene and metal using molecular dynamics simulations. In chapter 4, I will report on the ballistic transport in synthetic graphene. In chapter 5, I will discuss the optical transmittance and the layer counting method for graphene thin films. In chapter 6, the mechanical properties of graphpene, and its applications in Micro-electro-mechanical systems (MEMS), such as pressure and micro actuators will be discussed. In chapter 7, I will stress the optoelectronic applications for graphene, such as graphene plasmonics. In the final chapter, I will discuss the possibility and difficulty of graphene commercialization for industry.

CHAPTER 2

Graphene synthesis by chemical vapor deposition

2.1 Introduction

In the past decade, various graphene based applications have been proposed, for example: flexible and transparent touch screens [24], radio frequency integrated circuits [25], high power conversion efficiencies (15.6%) solar cells [26], and super-capacitors (specific capacitance: 502.78 F/g) [27]. To make these promising products into reality, the mass production of high-quality graphene is essentially required. Dozens of methods have been developed to produce graphene of various dimensions, shapes and qualities [28]. Table 2.1 lists the most commonly used methods for graphene production and the derived properties. Chemical vapor deposition has been widely accepted to be the most efficient and promising method to achieve large-scale and high-quality graphene films for optical and electronics applications in industry. In this chapter, I will introduce the principle of chemical vapor deposition, the homemade graphene growth furnace and the results of graphene growth.

Table 2.1: Properties of graphene films obtained by different methods [28].

Method	Carrier mobility (RT) (cm^2/Vs)	Sample size (mm)	Crystal size (μm)	Refs.
Mechanical exfoliation	$> 2 \times 10^5$	>1	>1,000	[3]
Molecular assembly	-	<0.001	<0.1	[29]
Epitaxial growth on SiC	1×10^4	100	50	[30]
Liquid-phase exfoliation	1-100	>1,000 (overlapped flakes)	0.1-100	[31]
Chemical vapor deposition	1×10^4	>1,000	>1,000	Ni [32] Cu [33] Ge [34]

2.2 Chemical vapor deposition

Chemical vapor deposition (CVD) is a chemical deposition process where chemical precursors are carried in the vapor phase and decomposed onto a heated substrate to produce high-purity, high-performance solid films [35]. CVD has become one of the most important methods to deposit films for the semiconductor industry due to its high throughput, high purity, and economic competitiveness. Furthermore, the CVD chamber is relatively simple and can be scaled up to fit large scale substrates. Monolayer graphene with size up to 30 inches has been produced by 8 inch quartz tube CVD furnace in 2010 [24].

Chemical vapor deposition (CVD) for high quality graphene growth was first reported with nickel as catalyst in 2009 [32] and later in the same year with copper as catalyst [33]. Multilayer or monolayer graphene can be achieved based on the solubility of carbon in these two metal catalysts. CVD is no longer a laboratory curiosity but has become the major technology to produce large scale graphene. 4 inch graphene films grown by CVD are currently available from commercial companies, for example: Graphene Supermarket, Graphene Square, Bluestone Global Tech, Graphenea, ACS Material, and CVD Equipment Corporation. The rapid development of the technology and the expansion of the market are expected to continue in the foreseeable future.

2.3 CVD furnace

Fig. 2.1 shows the schematic diagram of a CVD furnace for graphene growth. It can be divided in to three parts: Precursor gases supply, high temperature graphene reaction zone, and vacuum control system.

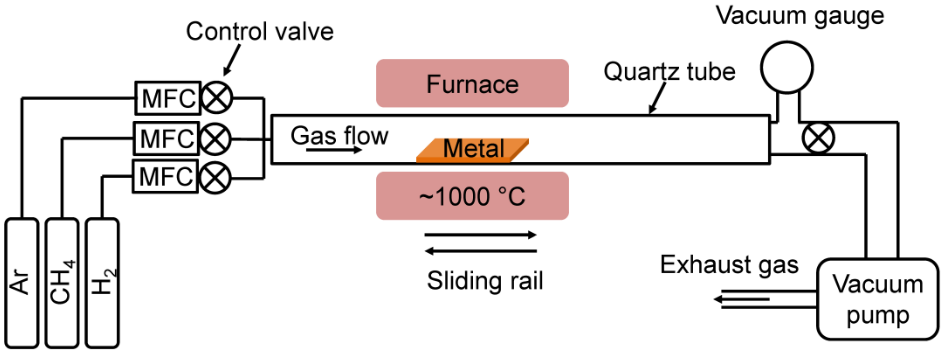

Figure 2.1: Schematic of thermal chemical vapor deposition system for graphene growth. Precursor gases (CH_4 and H_2) are carried by inert gas (Ar). The flow rates of gases are controlled by digital mass flow controllers (MFC). A quartz tube is used as the reaction chamber, and heated uniformly up to ~1000°C with a wire wound resistor furnace. The furnace is mounted onto a sliding rail for precise positioning of the center heating zone. A control valve and a vacuum gauge are used to regulate the base pressure of the growth chamber. The exhaust gases are diluted and pumped into an exhaust line.

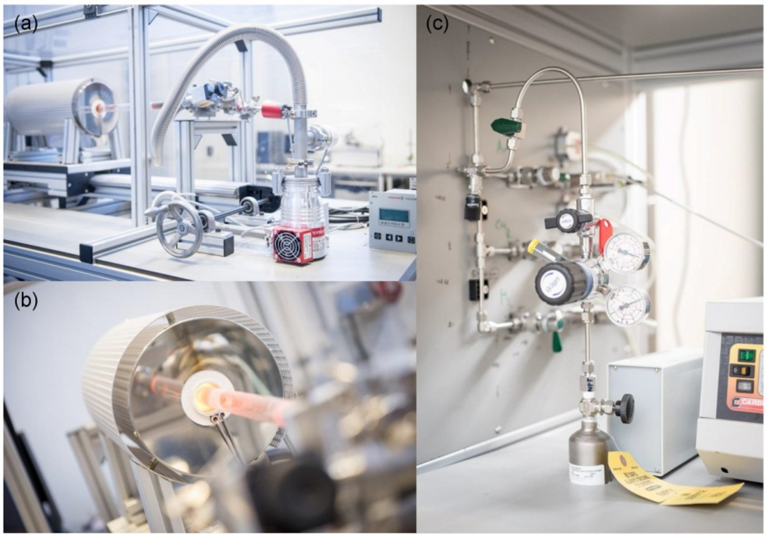

Figure 2.2: (a) An overview of the CVD furnace. The hand wheel is used to control the moving of the furnace. (b) The furnace heats the quartz tube and raises the temperature uniformly over 1000 °C. (c) The connection of the gas bottle.

A homemade CVD graphene growth system was designed and built as shown in Fig. 2.2a. The furnace (Carbolite TZF 12/38/400, maximum operation temperature 1200°C) was mounted onto a bench, with which the furnace is able to slide along a rail. Compared to a fixed furnace, the graphene growth time can be significantly reduced. A heating speed of 180°C/min (RT - 1000°C) and a cooling speed of 90°C/min (1000°C to 300°C) can be achieved, while the furnace maintains a fixed operation temperature. Fig. 2.2c show gas supply channels, where cylinder regulators (Linde REDLINE) are used to provide a reduced and constant gas pressure (cylinder pressure <200 bar) to the inlet of MFC and CVD chamber (working pressure <5 bar). Three MFCs (Bronkhorst EL-FLOW) powered by FLOW-BUS (Bronkhorst E-7000 FLOW-BUS power supply) are used to control the precursor gases (CH_4 0.1 - 5 sccm, and H_2 0.5 - 25 sccm) and carrier gas (Ar 6 - 300 sccm). An Oilless Dry Vacuum Pump (Pfeiffer ACP15 with pumping speed 15 m^3/h) connected to a turbo pump (Pfeiffer HiPace 80) is used to pump the exhaust gases and maintain the chamber base pressure less than 1×10^{-3} mbar.

2.4 Graphene growth

To achieve a clean growth environment, a dumpling-like copper pocket was made as shown in Fig. 2.3. It was shown that the graphene grown inside the pocket has much higher quality than that grown outside [36]. It would be advisable to use diluted nitric acid (~5 wt%) for ten minutes to clean the copper if there is any chromium-zinc anti-tarnish coating.

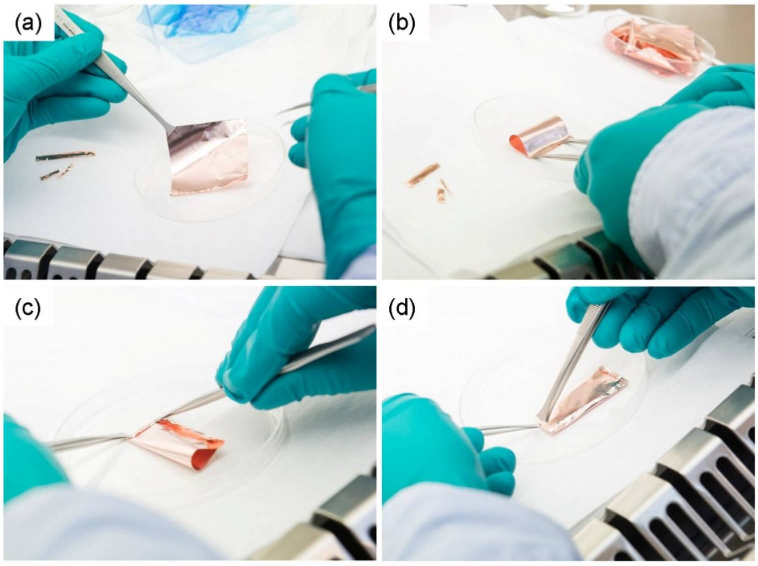

Figure 2.3: (a) Start with a piece of copper foil. (b) Fold the foil and clamp the edge along its long dimension. (c) Close one end of pocket by folding the edge (d) Close another side of the foil and form a dumpling-like pocket.

Fig. 2.4 illustrates the positioning of CVD furnace during growth and the temperature profile for one cycle of the graphene growth. A folded copper foil was inserted to a tubular quartz tube. Then, the CVD furnace was heated up to 1050 °C with flowing gases of H_2 and Ar (2 : 50 sccm), however, the foil was kept away from the heating zone of the furnace as shown in Fig. 2.4b. Once a constant temperature was reached (~ 1 hr), the furnace was moved to the position where the copper foil can be heated up to a uniform temperature as shown in Fig. 2.4a. The foil will reach ~1050°C within 15 min indicated in the temperature profile of Fig. 2.4d. After extra 15 min temperature stabilization, the gas mixtures ($CH_4 : H_2 :$ Ar = 0.5 : 2 :

50 sccm) were injected into the chamber for 30 min to allow the nucleation of graphene and crystal growth at a pressure of ~0.15 mbar. After graphene growth, the furnace was moved back to its original position, and the copper foil will be cooled down rapidly to prevent the further growth of graphene. Compared to temperature profile of the fixed furnace, the efficiency of graphene growth can be over 5 times improved. Further characterization of grown graphene will be presented in chapter 3.

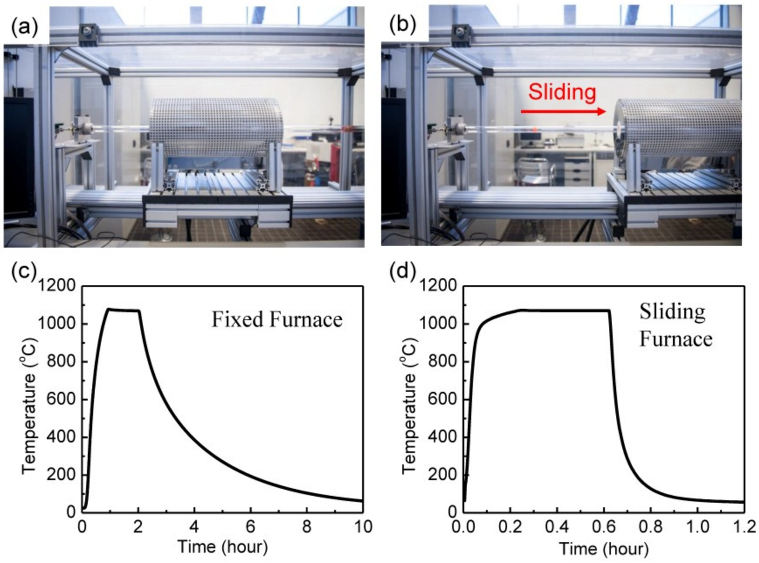

Figure 2.4: (a) A CVD furnace sitting in the graphene sample growth position. (b) A CVD furnace was slid away from the sample to achieve a fast cooling speed. (c) The temperature profile starts from heating till cooling with the furnace fixed in one position. (d) The temperature profile with sliding furnace.

CHAPTER 3

Molecular dynamics simulation of graphene on Cu

T. P. C. Klaver, Shou-En Zhu, M. H. F. Sluiter, G. C. A. M. Janssen

(Published in Carbon 82, 538-547 (2014))

We present results of molecular dynamics simulations of graphene on Cu surfaces. Interactions were modelled with the Charge Optimized Many Body potential, which gives a reasonable though not flawless description of the graphene-Cu system. The interaction between Cu and complete graphene sheets is characterized by an ‘averaged out’ interaction at a large bonding distance. Many bonding characteristics are indifferent to the details of how the Cu surface atoms are arranged, including the surface orientation and even if the surface is solid or molten. Graphene edges have a strong interaction with the Cu substrates. Systems were modelled at various temperatures, ranging from 0 K to the Cu melting temperature. At high temperature we find that the presence of graphene slightly stabilizes the Cu surface and retards surface melting. After cooling down to room temperature, the Cu substrate is 1.7% smaller than the graphene due to different thermal expansion coefficients. This leads to the formation of wrinkles in graphene. Single wrinkles experience only small migration barriers and are quite mobile. When multiple wrinkles intersect, they form immobile knots that hinder further movement of the connected wrinkles. The elastic energy of the wrinkles and knots due to bending of the graphene is determined.

3.1 Introduction

The extraordinary properties of graphene have lead to a very large amount of research on the topic after the publication of the landmark work [3] by Novoselov *et al*. Many different experimental methods, theoretical models and simulation techniques have been employed to study the properties of graphene. Apart from studying the properties of isolated graphene sheets, their production has also been the subject of extensive research. While early experiments used mechanical exfoliation with Scotch tape to produce single or few layer thick graphene samples, this process is not well suited for industrial production. Graphene growth through chemical vapour deposition (CVD) on solid surfaces or growth from C supersaturated substrates or through liquid phase exfoliation of graphite are much more promising methods in that respect. Despite the extensive research already done on CVD of graphene on Cu substrates, questions remain. Some observations have lead to conflicting explanations, while others are not explained very well at all. Some examples of such not yet (fully) resolved issues are the role of hydrogen in the gas mixture [37-39], the interaction of graphene with Cu under different orientations [40], the influence of temperature on growth [41] and the diffusion of C atoms and clusters during graphene growth [42]. Atomistic simulations offer detailed insight into processes occurring at atomic length and time scales. We have carried out classical molecular dynamics (MD) simulations of graphene on bare Cu (100) and (111) surfaces, to complement CVD-on-Cu experiments done in our group [43]. The empirical potentials required to model graphene on Cu must meet some rather tough requirements. In section 3.2 of this chapter we will explain our choice of the charge optimised many-body potential (COMB) [44, 45] and provide details of how simulations were carried out. In section 3.1 we first present and discuss results of how the COMB potential describes various properties of the graphene/Cu system. We then present simulations results of graphene on Cu at high temperature that is close to the melting temperature. Finally in section 3.3 we look at the graphene/Cu system once it has cooled down, and a size mismatch between Cu and graphene must be accommodated. The excess graphene resulting from the size mismatch leads to the formation of wrinkles. We compare the wrinkles observed in our simulations to similar types of wrinkles seen in experiments. A summary is given in section 3.4.

3.2 Computational details

Atomistic modelling of graphene-on-Cu requires an interaction potential capable of describing different types of interactions. It involves metallic interaction for Cu, covalent interaction for graphene, and weak van der Waals interaction between complete graphene layers and Cu. Of these interactions, the Cu-Cu interaction is commonly described by an embedded atom method (EAM) potential [46, 47], the C-C interaction is most often described by the widely used REBO2 [48] or AIREBO [49] potentials and the van der Waals interaction is often modelled by a Lennard-Jones (LJ) potential. The combination of using REBO2/AIREBO for modelling graphene and LJ bonding of the graphene to a solid surface is commonly used [50-55] and would also be sufficient for our simulations of complete graphene monolayers on Cu surfaces. However, this approach does impose restrictions. While complete graphene sheets only interact with the Cu surface through weak van der Waals interaction, C atoms on the edges of graphene islands have unsaturated bonds that can have a strong interaction with the Cu surface. Hence, the C-Cu interaction should ideally be capable of reproducing both of these different interaction regimes, so that graphene islands can be simulated. If graphene islands are grown through chemical vapour deposition with a methane feedstock, as is done in our group, simulation of such growth would require that C-H and Cu-H interactions are both reproduced by the potential as well, in both the van der Waals and chemical interaction regimes. Additionally, experiments that are not carried out in ultra-high vacuum with purified gasses will include small amounts of oxygen that rapidly interacts with the Cu surface. So ideally, the interaction potential should describe the elements C, Cu, H, and O and all cross interactions between these elements, in different bonding regimes for some element combinations. This is a tall order for any interaction formalism.

Two somewhat recently developed interaction schemes that aim to model a variety of interaction types for a range of elements are the reactive force field (ReaxFF) and COMB formalisms [56]. Both schemes include bond order and variable charge terms, giving them considerable versatility and thus making them promising candidates for modelling the required interactions. However, Wei *et al* [57] benchmarked various potentials for graphene against density-functional theory (DFT) data and found that the ReaxFF potential performed poorly. By contrast, the REBO2 potential performed quite well and the third generation of the COMB potential (COMB3) [44, 45] uses the REBO2 C-C interaction at shorter distances. Also, a parameterisation of the COMB3 formalism has already been successfully used to study hydrocarbons on Cu surfaces [44] as well as surface oxidation of Cu [58]. The parameterisations for C, Cu, H, and O within the COMB3 formalism should therefore allow the simulation of complete graphene sheets on Cu in this work, as well as extending the scope of the simulations to include H and O in future work. For these reasons, we used the COMB3 formalism, as implemented in the widely used MD code LAMMPS [59] in all our MD simulations.

Simulations of Cu surfaces covered by graphene had periodic in-plane dimensions ranging from 46.927 by 54.147 Å^2 to 504.56 by 504.56 Å^2. Simulation temperatures ranged from 0 K to our maximum experimental temperature of 1323 K (1050 °C). If the average thermal expansion coefficient (TEC) of Cu is estimated to be $1.7*10^{-5}$ in the 300-1323 K range (extrapolated from experimental data for 77 to 973 K [60]), heating Cu from 300 to 1323 K will cause 1.7% expansion. Therefore, three different, fixed Cu lattice parameters were used for simulations at different temperatures. At 0 K, the equilibrium parameter of 0 K was used, from 300 to 500 K the equilibrium lattice parameter at 300 K was used and at temperatures between 1140 K and 1323 K, the equilibrium lattice parameter at 1323 K was used. In contrast to Cu, graphene has a small TEC [17, 61]. At low temperature its in-plane lattice spacing can even slightly contract with rising temperature, despite increasing C-C bond lengths [62]. Therefore its thermal expansion was neglected and the 0 K equilibrium lattice parameter was used at all temperatures. In choosing surface areas, the number of Cu and graphene unit cells was chosen such that graphene could fit on the Cu with minimal misfit, if the simulation meant to portray stress-free graphene on Cu. The atoms in the bottom layer of the Cu slabs were held fixed to hold the slab and graphene layer on top of it in position. The Cu slabs consisted of 16 Cu monolayers or more. The numbers of Cu and C atoms varied from 6240 and 968 in the smallest system to 627200 and 99840 in the largest. A Nosé-Hoover thermostat was employed to simulate a canonical ensemble (NVT) in MD simulations. The fixed atoms in the Cu bottom layer were excluded from temperature control and reporting. The time step in MD simulations was 0.5 fs, which was small enough for results not to change noticeably when the time step was doubled in a few test simulations. The maximum simulation time was 2 ns. Analysis of surface melting in high temperature simulations was done simply through visual inspection with Ovito [63].

3.2.1 COMB3 description of the graphene/Cu system

Various properties of graphite and Cu were included in the fitting data for the COMB3 potential. The graphene lattice parameter of 1.42 Å is correctly reproduced by the potential. The experimental cohesion energy per C atom in graphite is 7.37 eV and the COMB3 potential predicts a slightly lower cohesion energy of 7.35 eV/C in an isolated graphene sheet. The 3.58 eV/atom cohesion energy and 0 K lattice parameter of 3.61 Å predicted for Cu agree well with the experimental values of 3.54 eV/atom and 3.62 Å [58] to which the potential was fitted. At 300 K and 1323 K, the Cu lattice parameter was 3.63 and 3.70 Å respectively, giving a linear TEC of $1.9*10^{-5}$ in that temperature range, in reasonable agreement with the average extrapolated experimental value of $1.7*10^{-5}$ [60]. The Cu melting temperature was determined through the coexistence method, i.e. running a constant energy simulation of an initially half crystalline, half molten system, where the melting temperature is reached when the molten/solid interface has stopped moving. The Cu bulk melting temperature within the COMB3 model lies between 1140 and 1145 K. This is over 200 K below the experimental melting temperature of 1358 K. This deviation is more than three times larger than for the computationally much cheaper EAM Cu potential distributed with LAMMPS, which resulted in a Cu melting temperature between 1290 and 1300 K. The calculated Cu (100) and (111) surface energies of 1.52 and 1.27 J/m^2 are somewhat lower than the orientation-averaged experimental value of 1.78 J/m^2 [64]. Our calculated graphene armchair edge energy was slightly higher than the zigzag edge energy (1.27 vs 1.13 eV/ Å), while DFT calculations [65] showed the zigzag edge energy to be higher (1.21 vs. 1.37 eV/ Å).

Beyond pure elements data, we have relaxed nearly stress-free graphene on Cu (100) and (111) surfaces at 0 K. We find that the interaction between graphene and Cu is one that has a fairly large equilibrium distance and that there is no strong interaction between pairs of individual C and Cu atoms. Instead, the interaction is more ‘smeared out and generic’ over larger numbers of atoms, where every C atom interacts with a number of Cu atoms that are at an approximately similar distance and *vice versa*. The resulting bonding between graphene and Cu surface is not very strong and mostly one-dimensional, perpendicular to the Cu surfaces. This picture agrees well with the observation that graphene binds to Cu only weakly [40, 66-69] through physisorption and that graphene (once formed, nucleation and growth may be influenced) is indifferent to the fine details of atomic arrangement of the Cu surface [70].

Even when allowed to fully relax, graphene sheets remained quite flat, not just on close-packed (111) surfaces but also on the more open (100) surfaces where C atoms do not sink significantly into openings between Cu atoms. Because of the generic nature of the interaction, results for both surface orientations are quite similar. The indifference of the graphene layer to which Cu orientation it binds, suggests that different in-plane orientations of the graphene with respect to one particular Cu surface would also not make much difference. This may seem to run counter to the observation that graphene can grow on Cu in preferred orientations [71]. However, it has been suggested [40, 72, 73] that the preferred orientations are determined (in the very early stages of graphene island growth) by the alignment between island edge atoms with unsaturated bonds and rows of Cu surface atoms. Thus, preferred orientations of graphene on Cu surfaces need not necessarily contradict the finding that large graphene islands would be rather energetically indifferent to their in-plane orientation.

Table 3.1: Cu-graphene binding distance d, binding energy per C atom E_b, charge accumulation per C atom q_C, maximum height variation for C atoms Δh_C and maximum height variation for Cu surface atoms Δh_{Cu} for graphene on Cu (111) and (100) surfaces, along with electronic structure values from literature for Cu (111).

property	on Cu(111)	electronic structure data on Cu (111)	on Cu(100)
$d_{Cu\text{-}graphene}$ (Å)	3.26	3.58 [a] 3.25 [b] 3.26 [c]	3.22
E_b/C atom (eV)	0.084	0.033 [c] 0.062 [b] 0.038 [a]	0.086
q_C (e^-)	0.04	0.008 [c] 0.004 [a]	0.04
Δh_C (Å)	< 0.01		< 0.02
Δh_{Cu} (Å)	< 0.01		< 0.01

[a] [68] [b] [74] [c] [69]

The binding distance is in either reasonable or excellent agreement with electronic structure results. The binding energy is always higher but still of the same order of magnitude compared to electronic structure data. The charge transfer to the C atoms is an order of magnitude greater than that predicted by electronic structure calculations. We also found that putting a net 0.1 electron charge per C atom in isolated graphene increases the C cohesion energy (i.e. lowers total energy) by 0.3 eV/C atom, which appears unlikely. While systems with net charge are not relevant to our work and probably lie outside what the COMB3 model was constructed for, it does demonstrate a broader tendency of graphene atoms to 'over-zealously' accumulate electronic charge in the COMB3 model. In compensation of the charge on the C atoms, the first few Cu surface layers show an alternating charge depletion/accumulation pattern that rapidly decreases in magnitude deeper into the Cu. The C/Cu areal density ratio is higher for the (100) orientation than for the (111) orientation (2.48 vs. 2.16) and this is reflected in the charge depletion of the Cu surface layers. On the

(100) orientation, the charge depletion on Cu atoms in the surface layer is 0.09 electron while on the (111) orientation it is 0.06 electron per Cu atom. The height variation for graphene on Cu is smaller but comparable to the variation of 0.04 Å found for graphene in one particular orientation on Ir, to which graphene also binds weakly [75].

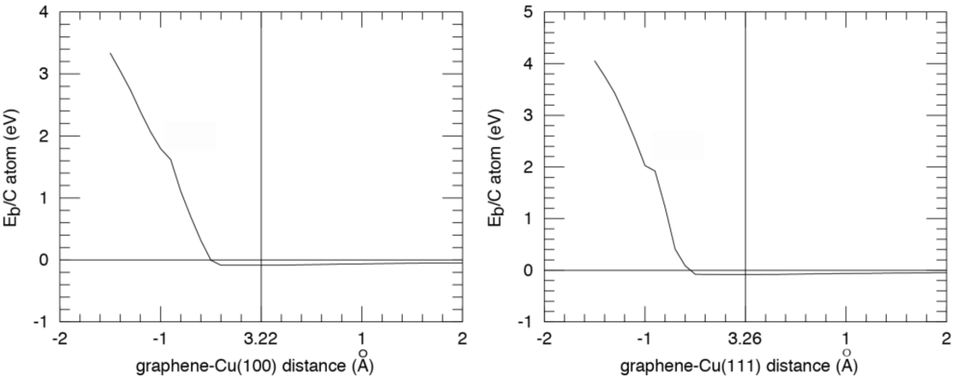

Figure 3.1: Interaction energy between graphene and Cu surface as a function of graphene-Cu distance. (a) on Cu (100). (b) on Cu (111).

Fig. 3.1 shows some features of the C-Cu bonding that seem incorrect. We know of no physical explanation for the shoulder present at ~1 Å compression and suspect that it is an artefact of the COMB3 potential. From ~0.5 Å closer to 2 Å further from the surface than the equilibrium distance, the slope of the energy is almost flat. As a result, the distance between the graphene and Cu surface may vary considerably with very low energetic cost. The cohesion energy curve calculated with the Random Phase Approximation shows no shoulder and has a much smoother LJ like shape [74]. Also, around 1.5 Å compression the energy curves do not increase more steeply with decreasing distance, as would be expected. For the (111) surface it even levels off slightly. Although the potential certainly has some shortcomings upon closer inspection, the COMB3 model produces graphene that binds to the Cu surface at a very reasonable distance and with a cohesion energy that is of the right order of magnitude. This makes the COMB3 model broadly suitable for our purposes.

3.2.2 High temperature simulations

Cu (100) and (111) surfaces were annealed up to 2 ns at various temperatures to see at which temperature the substrate would start melting within the short simulation time. For the more open (100) surface the temperature hardly needed to be above the bulk melting temperature. At 1145 K, the substrate had already melted to just above the locked bottom layer in 1.2 ns. By contrast, the close packed (111) surface did not show melting yet after 2 ns if the substrate was held at 1180 K. If held at 1190 K, there was a period where little seemed to happen until there was a melt nucleation event and then the whole substrate very quickly melted almost down to the locked bottom layer. While the observation that the (111) surface forms a greater barrier to melting than the (100) surface makes sense, the big difference in the required overheating is very much an artefact of the requirement that melting starts within the short, 2 ns simulation time. At longer time scales, the melting temperature for the (111) surface would draw much closer to that of the (100) surface.

The binding of graphene to Cu was hardly any less for molten surfaces than for solid surfaces (0.080 eV/C atom on molten Cu compared to 0.086 eV/C on Cu (100) and 0.084 eV/C on Cu (111)), again confirming the indifference of complete, large graphene sheets (nucleation and growth may be different) to the fine details of the underlying Cu surface.

Cu surfaces that were only half covered with graphene were annealed above the melting temperature. The presence of the graphene provides a modest amount of extra cohesion to the surface. The extra cohesion counteracts the melting of Cu. Therefore, in some of our simulations the bare part of the Cu surface had already molten almost down to the locked bottom layer while under the graphene the crystalline planes still reached almost to the surface. This was observed for graphene partially covering both (100) and (111) surfaces, see Fig. 3.2.

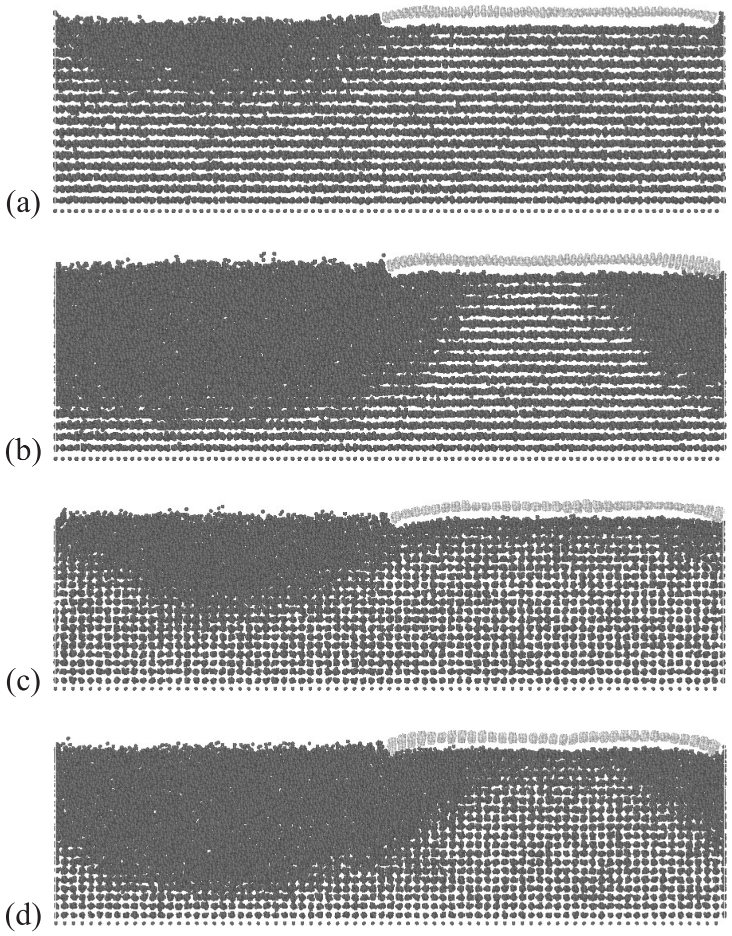

Figure 3.2. Melting of Cu (111) and (100) surfaces, half-covered with graphene. a, b: stages of Cu (111) melting. c, d: stages of Cu (100) melting.

Given that the simulation temperatures for both the systems in Fig. 3.2 are above the bulk melting temperature (a few K for Cu (100), tens of K for Cu (111)), both Cu substrates eventually melt down to the locked bottom layer, also under the graphene. However, we can well imagine that in experiments a narrow temperature window exists where the presence of graphene permanently tips the Cu surface from molten to solid. Graphene can be grown on molten Cu [41]. However, we think that in cases where the temperature in such experiments was barely above the melting temperature, a reassessment might be in order. There might be a narrow temperature window where graphene might grow on molten Cu, but that once formed, the graphene stabilises the Cu just enough to turn the surface solid.

It is noteworthy that the edges of the graphene layers in Fig. 3.2 are bending towards the Cu. This indicates that the COMB3 potential is producing a different bonding regime between Cu and graphene at the edge of the graphene sheet than it is producing in the middle of the sheet. In the middle there is only the weak van der Waals interaction as described in section 3.2.1, while at the graphene edges the interaction between C atoms with unsaturated bonds and the Cu surface is strong enough to make the sheet edge bend towards the Cu surface to shorten and further strengthen the Cu-C bonds. The edge type of the graphene sheet (zigzag on Cu (100), arm chair on Cu (111)) did not seem to have much influence on the results.

3.2.3 Room temperature wrinkle formation

In order to study what happens after cooling down, Cu (100) systems were created with graphene on them that was compressed 0.72 and 0.65 % or 1.43 and 1.36 % in the in-plane directions. In view of the similarity between Cu (100) and Cu (111) results, we only studied compressed graphene on Cu (100) surfaces. The (100) systems had surface areas a little under 13 x 13 nm^2. The graphene was initially a perfectly flat layer. Slowly cooling the system rather than creating the graphene with the complete strain in it would have been more realistic, were it not that cooling down over a 1000 K temperature range in the course of a simulation of some ns would always result in an unrealistically high cooling rate. The systems were simulated at room temperature for up to 0.5 ns.

In the system with the 0.72 and 0.65 % graphene compression, the graphene did not delaminate from the Cu. Apart from the normal, small thermal vibrations, the graphene remained flat. This agrees with the continuum elastic model by N'Diaye *et al* [76] which shows that a certain minimum strain threshold must be surpassed before it becomes energetically favourable to form wrinkles rather than keeping the graphene flat and compressed. By contrast, in the system where graphene was compressed 1.43 and 1.36 %, there was bending and buckling of the graphene at various places right from the start. In under 0.1 ns the bends and buckles had consolidated into a wrinkle which (forced by the period boundary conditions of the system, most likely) ran roughly parallel to one of the axes of the system. The very short time required to form the wrinkle seems to agree with observations for graphene on Ir by N'Diaye *et al* [76], who interpreted the sudden jump in low energy electron microscopy signals as the moment when suddenly graphene on cooling Ir goes from being flat to having wrinkles. A straight, 0 K relaxed piece of the wrinkle was 2.6 nm wide and 0.5 nm high. While on the whole the wrinkle ran parallel to one of the system axes, it contained some bends. Fig. 3.3 shows the 1.43/1.36 % compressed system after 0.22 ns.

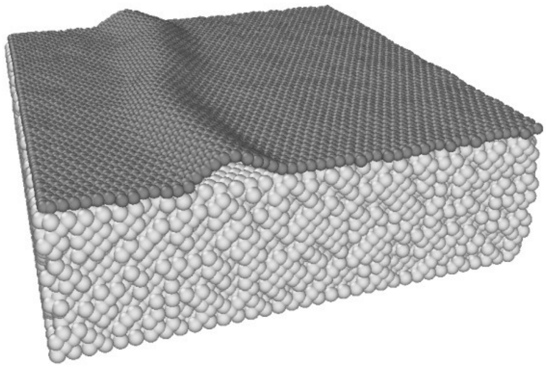

Figure 3.3: Graphene with 1.43 and 1.36 % compression on Cu (100), after 0.22 ns of simulation at 300 K.

The wrinkle that is shown in Fig. 3.3 was quite mobile. From the moment the separate bends and buckles had consolidated into the single wrinkle, it moved several nm within the tenths of ns duration of the simulation. The mobility of graphene wrinkles is in agreement with MD simulations by Guo *et al.* [55] of graphene wrinkles (induced by strains that seem questionably large to us) moving over graphite and Cu surfaces, under a thermal gradient. Both in our work and that of Guo *et al.* the mobility was probably higher than it would be in experiment, since it is much more likely to get a net movement over a relatively short wrinkle in a small simulation box than it is to get one for longer wrinkles in experiments. Still, the fraction of the wrinkle mobility that is present in experiments would provide a quick, easy mechanism for relieving strain in graphene by moving wrinkles to island edges where they can eliminate. The movement of our wrinkle was not uniform into one direction, but instead it moved up and down, seemingly randomly. The wrinkle also did not move uniformly as one fixed unit, but instead most of the wrinkle often moved in one direction, while (again seemingly randomly) a small part of it was standing still or moving in the opposite direction. As a result, the shape of bending of the wrinkle changed frequently as the wrinkle moved and the height and width also showed some variation around the values of 0.5 and 2.6 nm. While the particular motions of the wrinkles that we observed seemed random, the net movement of the wrinkle and movement in opposite direction by parts of the wrinkle was not coincidental. When the velocity components on the graphene atoms were randomly re-assigned from a Boltzmann distribution, the wrinkle started making similar sorts of movements again shortly afterwards. At present we have no good explanation for these wrinkle movements.

While the net mobility of the entire wrinkle in our simulations is likely higher than in experiments, the fluctuations within the wrinkle are probably more realistic. Since energy required to detach graphene from Cu at the front of a moving wrinkle is almost all gained back by re-attaching graphene to Cu at the back, the activation energy for movement would be very low.

The amount of elastic energy contained within the ripple could be determined from the potential energies of the individual C atoms. A Cu-graphene system with a wrinkle was cooled down to 0 K. Then the Cu substrate was removed. The potential energy of the atoms of the isolated graphene sheet, with no net charge on the C atoms, was then recalculated, see Fig. 3.4.

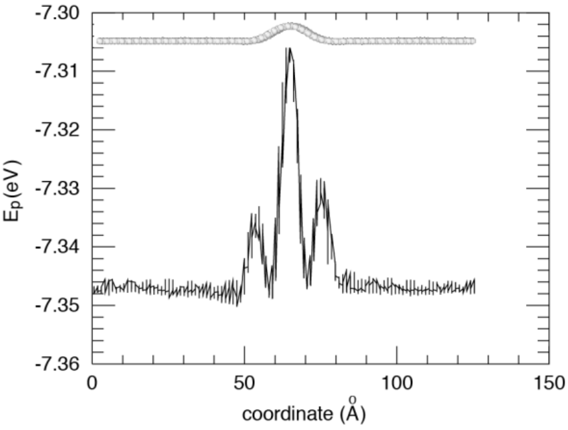

Figure 3.4: Potential energy of C atoms in an isolated graphene sheet with a wrinkle in it.

The atoms in the flat graphene left and right of the wrinkle all have a more or less similar potential energy, i.e. the cohesive energy of a C atom in flat graphene. Atoms inside the wrinkle are in energetically less favourable positions. The degree to which their potential energy is less negative than that of atoms in flat graphene is the bending energy. Hence the surface area of the peaks above the energy of atoms in flat graphene is the bending energy of the wrinkle, which turned out to be 1.6 eV/nm. This is less, but of the same order of magnitude as the wrinkle bending energy found by N'Diaye *et al* [76] in their model for graphene on Ir. Note that the wrinkle has two saddle points in the radius of curvature and that around those points the graphene in the wrinkle is flat. Hence, the potential energy of C atoms around these points drops down to the value of atoms in the flat graphene left and right of the wrinkle.

In addition to the wrinkle being roughly parallel to one of the system axes, the wrinkle is likely influenced by the periodic boundary conditions in other ways as well. There is a fixed amount of extra graphene that (apart from small residual strain after wrinkle formation) is accommodated into one wrinkle. This requirement means the height and width of the wrinkle will be influenced by the size of our periodic systems. When we doubled the size of the system in Fig. 3.4 in both dimensions, we still got a single wrinkle roughly parallel to one of the system axes but the width and height were approximately 3.6 and 0.8 nm and the bending energy was 1.9 eV/nm.

Having one bigger wrinkle with 1.9 eV/nm bending energy in the larger system is energetically much more favourable than having two smaller ones with bending energies of 1.6 eV/nm each. This shows an obvious driving force for consolidating smaller wrinkles into fewer, bigger ones, as was observed in few layer graphene on Ni substrates [77].

When we again doubled both the in-plane dimensions of our system, the result no longer was a single wrinkle. Instead, two wrinkles appeared under an angle with each other. The two wrinkles intersected to form a knot that immobilised both wrinkles, see Fig. 3.5.

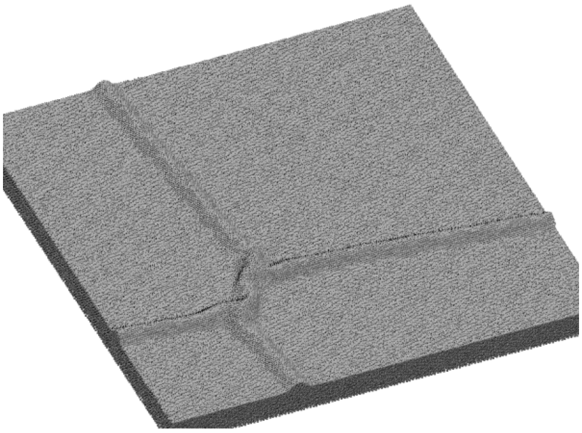

Figure 3.5: Cu (100) 505 x 505 Å^2 surface with graphene sheet on it under 1.43 and 1.36% compression. The knot that connects the two wrinkles immobilises them.

Once wrinkles had grown across the full length of the surface in two dimensions, they were held in place from two sides by the knot and its periodic images. From that time onward, the wrinkles straightened out and it was no longer the case that sections of the wrinkle moved up and down nanometers, while another section might be standing still or moving in the opposite direction. The energy of the knot structure can be determined similarly to how the bending energy of a wrinkle was determined in Fig. 3.4. First we determined the bending energy per length unit for a straight piece of the wrinkles in Fig. 3.5. Then we determined the wrinkle length in an area containing the knot, see Fig. 3.6.

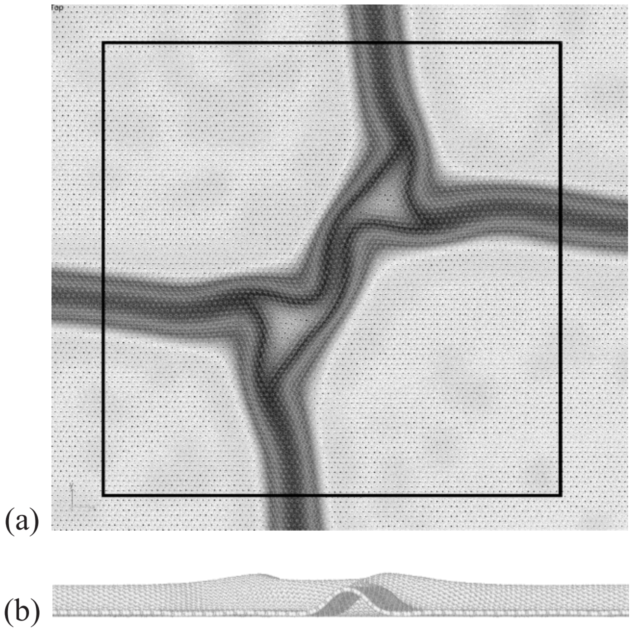

Figure 3.6: (a) Area of graphene containing knot of two wrinkles, coloured by height coordinate. The bending energy of the graphene inside the area marked with a rectangle was determined, see text. (b) Side view of graphene sheet with wrinkles and knot. The maximum height of the knot above the surrounding flat graphene was higher (1.6 nm) than the height of the straight wrinkles emanating from the knot (1.0 nm).

The bending energy of a straight piece of wrinkle was 2.3 eV/nm, the total wrinkle length in the area marked in Fig. 3.6 is ~36 nm. The bending energy of 36 nm of straight wrinkle would be 12 eV lower than the actual total bending energy we found for the graphene inside the marked area in Fig. 3.6. Hence the knot energy for the crossing of two wrinkles under an approximately straight angle is ~12 eV. Fig. 3.7 shows the knot area with atoms coloured according to their potential energy.

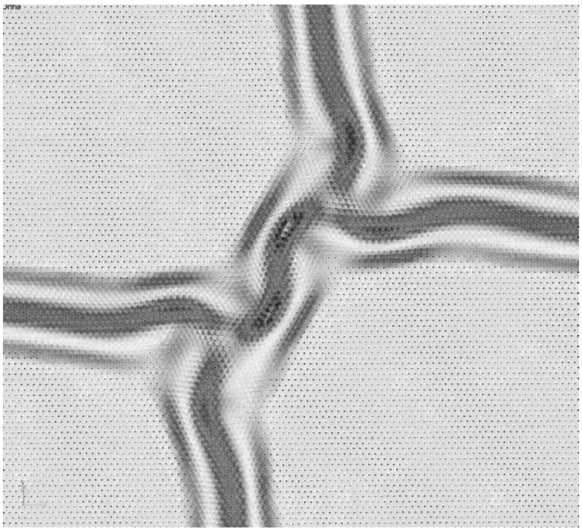

Figure 3.7: Area of graphene containing knot of two wrinkles, coloured by potential energy of the atoms. The parts of the knot that are highest above the Cu surface (see Fig. 3.6b) are not the ones with the highest potential energy, as the ‘domes’ do not curve very strongly. The atoms with the highest potential energy are located between the two domes, where the wrinkle forms a sharp fold.

While the high mobility of single wrinkles on flat surfaces has not been observed in experiments as far as we know (probably because catching moving wrinkles during their short mobile life times, before they eliminate at graphene island edges or form immobile knots, is quite difficult experimentally), immobilised wrinkles such as in Fig. 3.5 have been reported for (few layer) graphene on a number of different substrates, including Ir [75, 76, 78], Pt [77], Ni [77, 79], SiC [80] and, somewhat less clearly recognisable on rougher surfaces, on Cu [81] and Rh [82]. While the similarities between immobilised wrinkles in our simulation and in experiments is encouraging, there are also some differences. First, in our simulation the knot in defect-free graphene formed at an apparently random place on the perfectly flat surface, where the wrinkle ends happened to meet up. In experiments, wrinkle nucleation may happen around defects, such as heptagon–pentagon pairs in graphene [76], and is therefore more heterogeneous. Secondly, in experiments the wrinkles often intersect under angles of 120° or other angles different from the approximately straight angle in Fig. 3.5. This difference probably stems from an unphysical influence of the periodic boundary conditions in our systems.

The stable persistence of immobile wrinkles would take care of some of the 1.7% thermal expansion size difference between Cu and graphene that must be accommodated during cooling. Another part of the 1.7% remains as residual strain that remains after wrinkle formation, as observed on Ir surfaces [76, 78]. Indeed, in our experiments we see graphene sticking out ~0.8% from the deposition area after cooling down, rather than 1.7%.

3.3 Summary

We have carried out classical molecular dynamics simulations of graphene on Cu (100) and (111) surfaces. Correctly reproducing all interactions between elements involved in CVD growth of graphene on Cu (Cu, C, H and O) is a complex task for which currently only two interaction formalisms (that share a number of characteristics) are available, ReaxFF and COMB. The COMB3 formalism gives a reasonable description of the Cu-graphene systems, though it has a number of shortcomings too.

The bonding distance between Cu and complete graphene sheets is 3.2 Å and at that distance there are no clearly distinguishable pairs of interacting Cu and C atoms. Instead, each C atom interacts with a number of Cu atoms close in distance and *vice versa* through weak van der Waals interaction. The interaction is ‘averaged out’ and C atoms are mostly indifferent to the fine details of how the Cu surface atoms are arranged, such as the Cu surface orientation or whether the surface is solid or molten. At graphene edges the situation is very different. There the COMB3 formalism correctly shows a much stronger interaction between C atoms with unsaturated bonds and Cu surface atoms. This causes graphene edges to bend down towards the Cu.

The tens of meV of binding per C atom between complete graphene and the Cu surface slightly stabilises the Cu surface and retards surface melting. The simulations suggest that there is a narrow temperature window where the presence of graphene would keep the Cu surface crystalline where a bare surface would show surface melting.

Graphene layers under 1.4% compression showed the spontaneous formation of wrinkles. In simulation boxes of 13 x 13 and 25 x 25 nm^2 a single wrinkle appeared. Single wrinkles were quite mobile, moving several nm overall in tenth of ns of simulated time, in addition to smaller segments of the wrinkle moving up and down individually while other segments were standing still or moved in the opposite direction. The overall movement of wrinkles seen in our systems would be larger than in experiments, since it is easier to get a net overall movement over a short wrinkle length such as in our simulated systems. However, in experiments longer wrinkle sections would likely still have considerable mobility, since there is very little in the way of a migration barrier for graphene wrinkles to overcome. Energy required to detach graphene from the Cu surface at the front of a moving wrinkle is gained back by reattaching graphene at the back of the wrinkle. The elastic energy in the wrinkle was determined by detaching graphene and recalculating the potential energy of the C atoms. The degree to which the potential energy of atoms inside the wrinkle is less negative than that of C atoms in flat graphene, represents the bending energy. The bending energy depends on the system size (which, through the periodic boundary conditions, influences wrinkle height and width). For systems of 13 x 13 and 25 x 25 nm^2 we determined wrinkle energies of 1.6 and 1.9 eV/nm, showing that it is energetically favourable to consolidate multiple small wrinkles into a single bigger one. On a 51 x 51 nm^2 substrate, compressed graphene developed multiple wrinkles under an angle that linked up to form an immobile knot. The elastic energy of the knot structure was 12 eV. While the highly mobile single wrinkles in our simulations have not been observed in experiments as far as we know (possibly because their life times may be too small), immobilised wrinkles that are tied together under an angle have been observed in graphene on a number of different surfaces.

3.4 Acknowledgements

We thank Prashanth Srinivasan and Robbert-Jan Dikken for determining the EAM Cu melting temperature and Thomas Michely for helpful discussion and reading of the manuscript. This work is part of the research program of the Foundation for Fundamental Research on Matter (FOM), which is part of the Netherlands Organisation for Scientific Research (NWO).

CHAPTER 4

Ballistic transport in CVD graphene

Victor Calado*, Shou-En Zhu*, Srijit Goswami, Qiang Xu, Kenji Watanabe,
Takashi Taniguchi, G.C.A.M. Janssen, Lieven Vandersypen (* these
authors contributed equally)

(Published in Appl. Phys. Lett. 104, 023103 (2014))

In this chapter, we report the observation of ballistic transport on micron length scales in graphene synthesized by chemical vapour deposition (CVD). Transport measurements were done on Hall bar geometries in a liquid He cryostat. Using non-local measurements, we show that electrons can be ballistically directed by a magnetic field (transverse magnetic focussing) over length scales of ~1 μm. Comparison with atomic force microscope measurements suggests a correlation between the absence of wrinkles and the presence of ballistic transport in CVD graphene.

4.1 Introduction

High electronic quality in graphene is a key requirement for many experiments and future applications [28]. The highest quality has so far been achieved in exfoliated graphene [3], either by suspending the graphene flakes [22] or by depositing them on hexagonal boron nitride (hBN) substrates [83]. To move beyond a laboratory setting, mass production of graphene is essential. Among several promising synthesis methods, chemical vapor deposition (CVD) is a low-cost, scalable, and controllable method for the production of monolayer graphene [84, 85]. Using CVD, predominantly monolayer graphene of high quality has been synthesized on copper foils [33]. Considerable effort has been made to scale up the technology to produce meter-sized foils [24, 86] and to achieve crystals with mm dimensions [36, 87, 88]. Such large crystal sizes minimize short-range scattering from grain boundaries [89-92]. Also for CVD graphene, the highest electronic quality is realized by transferring it onto hBN [93, 94], using a clean (contaminant-free) and dry procedure [83, 95].

Despite this effort, the electronic quality of CVD graphene is still considered to be inferior to that of exfoliated graphene, and, in particular, there are no reports of ballistic transport phenomena in CVD graphene. Ballistic transport is of relevance for realizing electron optics experiments, such as Veselago lensing [96] and angle-resolved Klein tunneling [97] or specular Andreev reflection [98]. A negative bend resistance in a cross geometry [99, 100] gives a first indication of ballistic transport. A more sensitive probe, since it is more easily affected by small angle scattering, is transverse magnetic focussing (TMF), seen two decades ago in a GaAs/AlGaAs two-dimensional electron gas [101] and only recently in exfoliated graphene [102].

4.2 Graphene growth results

Following previous work [33, 36], a copper foil with a thickness of 25 μm is cut in ~2 × 3 cm^2 sheets (Alfa Aesar > 99.8% pure). The foil is folded to form a fully enclosed pocket and placed inside a quartz tube in a home built tube oven. 0.5 sccm CH_4 and 2 sccm H_2 are fed through the tube with a CH_4 partial pressure of less than 20 µbar. The temperature is set to 1050 °C, close to the Cu melting point. With these parameters, we obtain a low nucleation density in the inside of the foil pocket. In Fig. 4.1a, we show a scanning electron microscope (SEM) image of seven graphene crystals on copper spread over an area of 3.1×2.0 mm^2. This yields a nucleation density of ~1.1 mm^{-2}. With such a low nucleation density, we are able to grow crystals that have an average diameter of 1 mm. We used isolated crystals, formed in the early stage of CVD growth, such as the one shown in Fig. 4.1b. These crystals are about 150 µm across and are grown in about 30 min. The crystals have a sixfold dendritic shape. We note that at the nucleation site, a second layer starts growing.

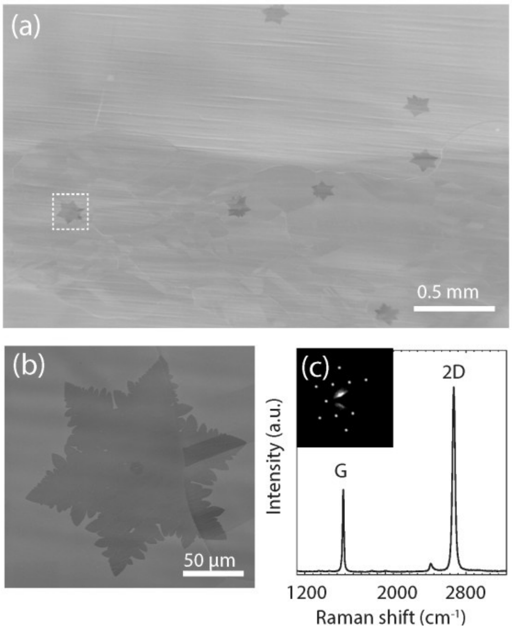

Figure 4.1: (a) SEM image of a copper foil with isolated graphene crystals after a short growth time. (b) A SEM image of one of the crystals in (a), where the dendritic shape at the edges is visible. The dark stripes are different crystal orientations in the Cu. (c) Raman spectrum taken of another graphene flake transferred from copper to SiO_2, grown in similar conditions. Inset: a typical diffraction pattern, recorded in a TEM.

In Fig. 4.1c, we show a Raman spectrum taken on a graphene crystal similar to those in Fig. 4.1a, after transfer to SiO_2. The spectrum confirms that the crystals are monolayer graphene [103] with a defect density below the Raman detection limit, as no D line at 1350 cm^{-1} is visible. In the inset of Fig. 4.1c, a transmission electron microscope (TEM) diffraction pattern is shown. It confirms a hexagonal lattice [104]. We have recorded many more diffraction patterns as shown in Fig. 4.2, which show the same lattice orientation over a distance of 50 μm. This indicates that the graphene patches in Figs. 4.1a and 4.1b are monocrystalline, i.e., have no grain boundaries.

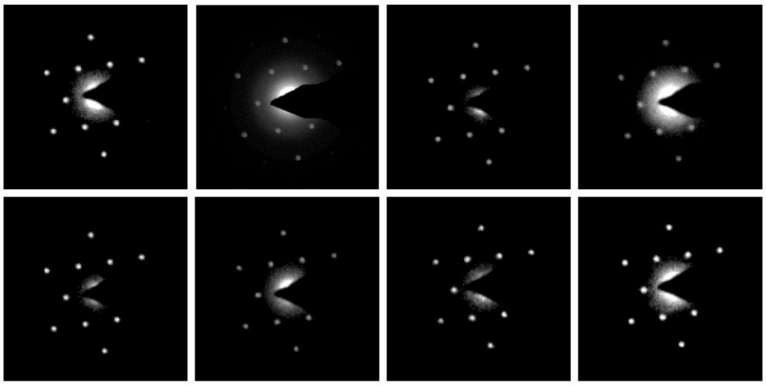

Figure 4.2: Eight diffraction patterns taken with TEM in different locations in the same graphene crystal.

4.3 Graphene transfer

Large grain size single crystals are grown on a folded copper foil enclosure and subsequently dry transferred onto hBN flakes. The outside has predominantly small crystals, which are removed by reactive ion etching in oxygen plasma. An Elvacite film (Elvacite acrylic resin 2550 dissolved in MIBK, ~100 mg/mL, Lucite International, Inc.) is spun on a CVD graphene/Cu foil, which will act as a polymer support, Fig. 4.3b. The Elvacite/CVD graphene/Cu foil is attached to a support frame by a polyamide adhesive, the support frame is not shown in the illustrations. The copper is dissolved in a 20 g/L ammonium persulfate ($(NH4)_2S_2O_8$, ACS reagent, ≧98.0%, Sigma-Aldrich 248614) solution for about 3 hours. The support frame is gently taken out of the etchant solution and dried. The result is a support frame with a free standing Elvacite/graphene film, illustrated in Fig. 4.3c without frame. This stack is transparent and is attached to the micromanipulator in a transfer setup and subsequently transferred onto hBN fakes as shown in Fig. 4.3d.

CVD graphene on copper is transferred onto a hBN flake. The hBN flakes are prepared by mechanical exfoliation on a polymer substrate. A 250 nm thick hBN is selected and transferred onto e-beam defined tungsten (W) gate electrodes, so that the hBN acts as a gate dielectric [95]. The tungsten can withstand high temperatures during annealing to remove residues from the hBN flake. Furthermore, the bottom gate screens charged impurities, presumably present in the SiO_2 below.

In Fig. 4.3e, an optical microscope image is shown of a device consisting of W bottom gates with hBN and CVD graphene transferred on top. An AFM image (Fig. 4.3f) reveals that a lot of residues are present after the transfer of graphene on hBN. Subsequent annealing in high vacuum (~10^{-6} mBar) at 600 °C yields a surface shown in Fig. 4.3g. Many bubbles are present that are interconnected with each other by wrinkles. Flat areas are present, where the surface roughness as measured by AFM is ~0.1 nm, similar to that of a clean bare hBN surface. To find out what is inside the bubble we performed (on other samples) an oxygen plasma etching step (using a Leybold Z400 with 20 W RF power and 25 sccm O_2 at 20 μbar for 30 sec.). This removes graphene, but the bubble shape persists. From that we deduce that inside the bubbles a solid substance is present. Measurements using contact mode AFM on bubbles show that the bubbles are only partly compressible, which is consistent with the presence of a solid substance inside [105]. Presumably residues in between the graphene and hBN are present and are mobilized during the annealing process coalescing and forming bubbles.

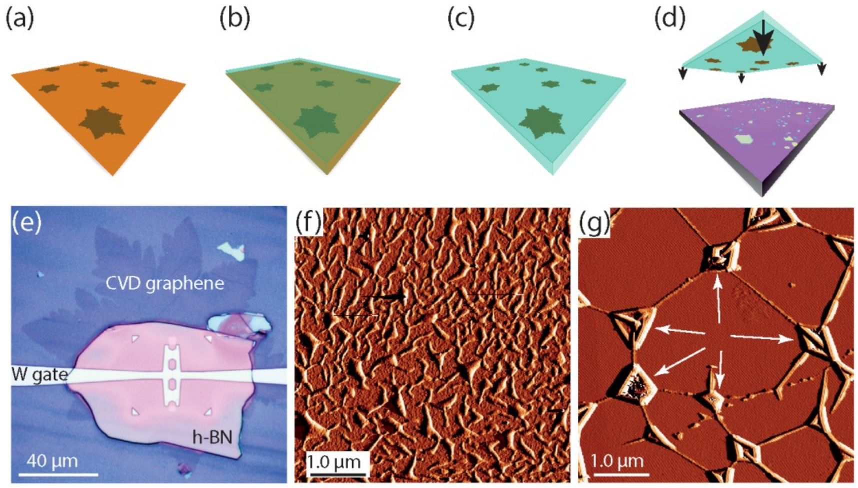

Figure 4.3: (a-d) Dry transfer process schematically shown in steps. (e) Optical microscope image of a CVD graphene crystal transferred onto a hBN fake with a W bottom gate. (f) AFM image of the surface of an as transferred CVD graphene crystal on hBN. A lot of residues are present. (g) AFM image of the same surface as in (f), but after annealing in high vacuum (~ 10^{-6} mBar) at 600 °C

4.4 Quantum transport measurement

We have contacted the CVD graphene flake with e-beam lithography defined 3 nm Cr/25 nm Au contacts (Fig. 4.4a) and subsequently etched Hall bars with reactive ion etching in oxygen. In Fig. 4.4b, we give a device schematic. Transport measurements were done in vacuum at 4K and at room temperature (RT). In Fig. 4.4c, we show the sheet resistance measured at 4K in black and at RT in cyan. The resistance peak at the charge neutrality point (CNP) became taller and narrower upon cooling as expected. We applied a 1 μA dc current bias across the Hall bar (in the inset) and measured the voltage between terminals L_1 and L_4 as a function of gate voltage on the tungsten bottom gate. The charge carrier density is tuned by the gate voltage with a coupling strength of $7.45 \pm 0.02 \times 10^{10}$ cm^{-2}V^{-1}, extracted from Hall measurements. We find the CNP is offset by only 3.31 $\times 10^{10}$ cm^{-2}, indicating very little background doping.

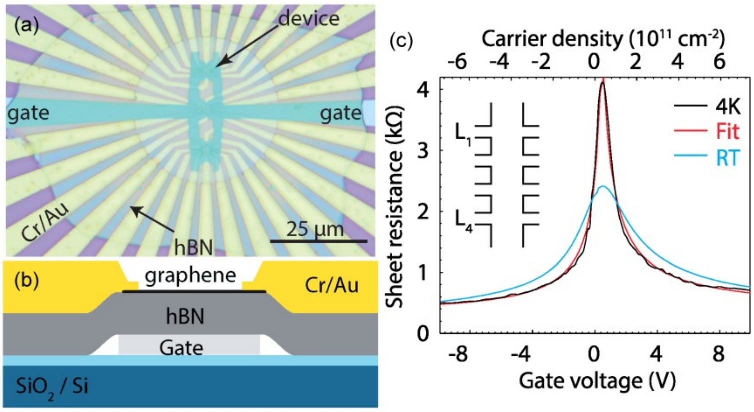

Figure 4.4: (a) Optical microscope image of the device. A hBN flake (light blue) is transferred onto a tungsten bottom gate. Yellow stripes are the gold contacts. They are deposited in two steps, with the outer part much thicker (~350 nm) than the inner part, leading to the circular pattern in the image. (b) A schematic side view of the device, with the materials indicated. The hBN acts here as a dielectric between the graphene and W bottom gate. (c) Black and cyan: the sheet resistance as a function of gate voltage and carrier density taken at 4K, respectively, room temperature between probes L_1 and L_4 (see inset). Red: a fit to the 4K data using the self-consistent equation for diffusive transport as a model.

We characterize the transport properties of the device by fitting the 4K data with the self-consistent Boltzmann equation for diffusive transport that includes long and short range scattering [106, 107]: $\rho = (ne\mu_c + \sigma_0)^{-1} + \rho_S$, where μ_c is the mobility from long range scattering, σ_0 the minimum conductivity at the CNP, and ρ_s the resistivity from short range scattering. This model fits very well to the data when we account for the electron-hole asymmetry by using different fit parameters for the two sides. For the low temperature hole mobility, we find μ_h = 41500 ± 800 $\text{cm}^2\text{V}^{-1}\text{s}^{-1}$, for the electron mobility, μ_e = 28700 ± 600 $\text{cm}^2\text{V}^{-1}\text{s}^{-1}$. The RT mobilities are about a factor two lower.

For the resistivity from short range scattering, we obtain $\rho_S = 280 \pm 10\Omega$ for holes and $\rho_S = 380 \pm 10\Omega$ for electrons. These are higher than what has been found earlier for exfoliated flakes on hBN (~70 Ω) [83]. For the residual conductivity σ_0, we find a value of 221 ± 1.5 µS, which is 5.70 ± 0.04 e^2/h. The mobility values found here are for long range scattering only. Using the Drude model of conductivity, one finds a mean free path of 200-400 nm for a density of 7×10^{11} cm^{-2}.

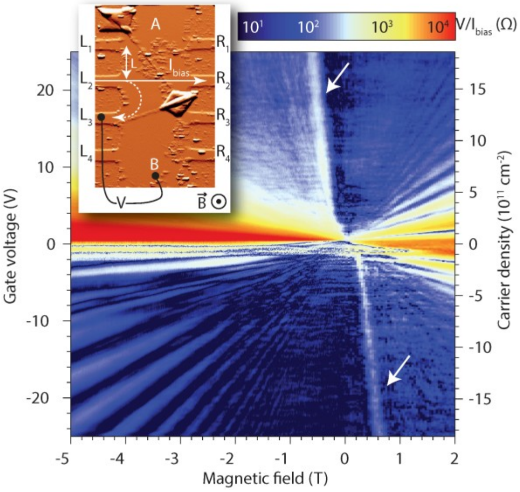

Figure 4.5: The resistance V/I_{bias} as function of gate voltage and magnetic field plotted in a logarithmic color scale. The straight lines are due to SdH oscillations and the square-root line is due to TMF, indicated by arrows. Inset: AFM image of the measured device, showing the non-local measurement configuration used for observing magnetic focussing. V is measured between L_3 and B, while a current bias is applied between L_2 and R_2.

Next, we test whether this device allows transverse magnetic focusing (TMF). The observation of TMF would directly imply the occurrence of ballistic transport in that part of the device. As shown in the inset of Fig. 4.5, we apply a magnetic field perpendicular to the device with a current bias from contact L_2 to R_2. The Lorentz force will act on the charge carriers and will steer them in a circular orbit with cyclotron radius $R_c = \hbar k_F / eB$, where R_c is the cyclotron radius. Electrons leaving contact L_2 can reach contact L_3 when the cyclotron radius matches one half the distance between the contacts L, provided the electrons are not scattered while traveling along the semi-circle joining the contacts. This focussing condition occurs for specific combinations of magnetic field and gate voltage

$$B = \frac{2\hbar k_F}{eL} \propto \sqrt{V_{gate}} \tag{4.1}$$

The momentum of the charges, $\hbar k_F$, is tuned with the bottom gate voltage V_{gate}.

When electrons reach contact L_3, its potential will be raised. We probe this potential by recording the voltage V between terminal L_3 and B, making the assumption that the potential of the far-away contact B remains constant. The gate voltage and magnetic field are swept and the resistance V/I_{bias} is plotted on a logarithmic color-scale in Fig. 4.5.

In Fig. 4.5, above fields of ± 1 T, Shubnikov-de Haas (SdH) oscillations are seen as straight lines diverging for larger magnetic field. However, the lines marked with white arrows do not fit the SdH pattern. These lines are attributed to TMF, following from the square-root dependence between the magnetic field and charge carrier density, see Eq. (4.1). For negative field and positive gate voltage, electrons leaving L_2 are deflected towards contact L_3, where an increase in the voltage V is observed. For positive field and negative gate voltage, we find the same square-root dependence, where holes are deflected instead of electrons. Such behavior can only be observed when the region between the contacts permits ballistic transport, i.e., little scattering takes place. The fact that the focussing signal appears only for a specific combination of magnetic field and gate voltage, giving rise to a sharp peak in the plot, illustrates the sensitivity of the focussing effect to scattering: only small deviations away from the proper semi-circular path are enough to make electrons miss contact L_3.

From a fit to the data, we find a distance of L = 570 nm, which corresponds to a semicircle distance of ~900 nm that electrons have travelled. This value is somewhat larger than the expected lithographic distance of 500 nm. A similar mismatch between the extracted contact separation from TMF and the lithographic distance was recently reported in exfoliated graphene [102]. In these experiments, TMF peaks were seen also at integer multiples of the B value given in Eq. (4.1). The absence of such peaks in our measurements suggests that the edges in our sample are too rough or dirty to allow specular reflection.

We have performed analogous measurements across the entire device and except between L_1 and L_2 no focussing was found, pointing at the presence of inhomogeneities. In the inset of Fig. 4.5, we show an atomic force microscope (AFM) image of the device. In the device, a bubble and two wrinkles are present, which may hinder transport. The wrinkles are 1–2 nm in height and less than ~40 nm in width (not accounting for convolution with the AFM tip width). The bubbles are about ~35 nm high. The apparent connection between the absence of wrinkles or bubbles and the observation of TMF in this device indicates that is worth investigating more systematically whether such wrinkles and bubbles are sufficient to spoil ballistic effects. We note that given the presence of the wrinkles and bubbles in the Hall bar, the mobility values are remarkably high, in the range of the highest reported mobilities in CVD graphene [93].

4.5 Conclusion

In summary, we have demonstrated that TMF can be observed in CVD graphene on a micron scale distance. The CVD process was optimized to obtain large single crystal flakes. In order to preserve its high quality, we have transferred graphene flakes with a dry method onto hBN. The main limitation in electronic quality for the current device appears to be the presence of wrinkles and bubbles. If one optimizes further the processing to reduce or eliminate the wrinkles and bubbles, it may become possible to routinely observe ballistic phenomena in CVD graphene. Already, the present results are an important step forward in the direction of scalable and controllable graphene production not only for industrial applications but also for fundamental research involving ballistic effects in graphene.

4.6 Acknowledgement

We thank A. M. Goossens for discussions and R. Schouten, R. Luttjeboer, P. van Holst, H. Jansen, and L. Schipperheijn for technical assistance. We thank G. F. Schneider and S. R. K. Malladi for preparing the TEM sample and H. Zandbergen for providing access to the TEM setup. We acknowledge the Young Wild Idea Grant from the Delft Centre for

Materials (DCMat) for financial support. This work is part of the research program of the Foundation for Fundamental Research on Matter (FOM), which is part of the Netherlands Organization for Scientific Research (NWO).

CHAPTER 5

Optical transmittance of multilayer graphene

Shou-En Zhu, Shengjun Yuan, G.C.A.M. Janssen

(Published in EPL (Europhysics Letters) 108, 17007 (2014))

We study the optical transmittance of multilayer graphene films up to 65 layers thick. By combing large-scale tight-binding simulation and optical measurement on CVD multilayer graphene, the optical transmission through graphene films in the visible region is found to be solely determined by the number of graphene layers. We argue that the optical transmittance measurement is more reliable in the determination of the number of layers than the commonly used Raman Spectroscopy. Moreover, optical transmittance measurement can be applied also to other 2D materials with weak van der Waals interlayer interaction.

5.1 Introduction

Graphene is a two-dimensional material with carbon atoms in a honeycomb lattice. It has many potential applications thanks to its unique electrical, mechanical, chemical and optical properties [10, 108, 109]. Graphene may outperform existing transparent conductive materials, and a graphene based flexible touch screen was demonstrated by Bae *et al.* in 2010 [24]. Multilayer graphene is a graphene thin film with weak van der Waals interaction between the layers, and its electronic and optical properties are sensitive to the number of layers as well as the stacking sequence [10, 108]. A fast and reliable method to determine the layer number is desired in the fabrication and measurement of multilayer graphene.

For multilayer graphene, Min *et al*. derived that the optical transmission through a graphene films is directly dependent on the optical conductance of the graphene stack, and the optical transmittance $T(\omega)$ of graphene films as a function of incident light frequency ω can be written as [110, 111]:

$$T(\omega) = \left[1 + \frac{2\pi}{c} G(\omega)\right]^{-2} \tag{5.1}$$

where $G(\omega)$ is the optical conductivity of the graphene film, and c is the speed of light. In the visible region, by neglecting the interlayer interaction, the optical conductivity of multilayer graphene is linearly proportional to the layer number N as $G(\omega) = NG_1(\omega)$, where $G_1(\omega)$ is the optical conductivity of single layer graphene at frequency ω *[110]*. $G_1(\omega)$ only becomes equal to the universal optical conductance $G_0 = e^2/(4\hbar)$ in the limit of a massless Dirac fermion bandstructure [108, 112], where e is the elementary charge, and $\hbar$ is the reduced Planck constant [110, 113]. The optical transmittance of multilayer graphene can be simplified to:

$$T(\omega) = \left[1 + \frac{2\pi}{c} NG_1(\omega)\right]^{-2} \tag{5.2}$$

where $G_1(\omega) = f(\omega)G_0$. $f(\omega)$ is a correction coefficient to compensate the deviation between $G_1(\omega)$ and G_0. The Eq. (5.2) can be further revised including the well defined value G_0 as:

$$T(\omega) = (1 + f(\omega)\pi\alpha N/2)^{-2} \tag{5.3}$$

here, $\alpha = e^2/(\hbar c) \approx 1/137$ is the fine structure constant [20]. Previous work from Nair *et al.* has shown that monolayer graphene can absorb ~2.3% of light. This value is $\pi\alpha$ based on the Dirac cone approximation, which is only valid for the coupling between light and relativistic electrons near the Dirac point [20].

5.2 Numerical simulation

In order to obtain more reliable theoretical results of optical conductivity by considering interlayer hopping as well as a different stacking sequence in multilayer graphene, we carried out large-scale simulation in the framework of the full π band tight-binding model. The optical conductivity $G(\omega)$ is calculated numerically by using the Kubo formula [114-116] (omitting the Drude weight which is not related to the light adsorption at finite ω),

$$G(\omega) = \lim_{\varepsilon \to +0} \frac{1 - e^{-\beta\hbar\omega}}{\hbar\omega A} \int_0^\infty dt e^{i(\omega + i\varepsilon)t} 2i \operatorname{Im}\langle \phi | J[1 - f(H)]J(t) f(H) | \phi \rangle \tag{5.4}$$

where A is the sample area, $\beta = 1/T$ is the inverse temperature, $f(H) = 1/\{\exp[\beta(H - \mu)] + 1\}$ is the Fermi-Dirac function of the Hamiltonian operator H, μ is the chemical potential, and J is the current operator [115]. The state $|\phi\rangle$ is a normalized random state which covers all the eigenstates in the whole spectrum. The time evolution operator and Fermi-Dirac operator are represented as Chebyshev polynomial expansions [115]. In order to phenomenologically implement the red shift of the absorbance spectrum due to the excitonic effect, the hopping energy between two nearest atomic sites is reduced to be $t = 2.3$ eV, the value which leads to the match of the simulated π-excitonic peak at $2t$ and the experimetnal observed peak at 4.6 eV. The numerical method implemented here has the advantage that the CPU time and the memory costs in the simulations are both linearly dependent on the size of the sample.

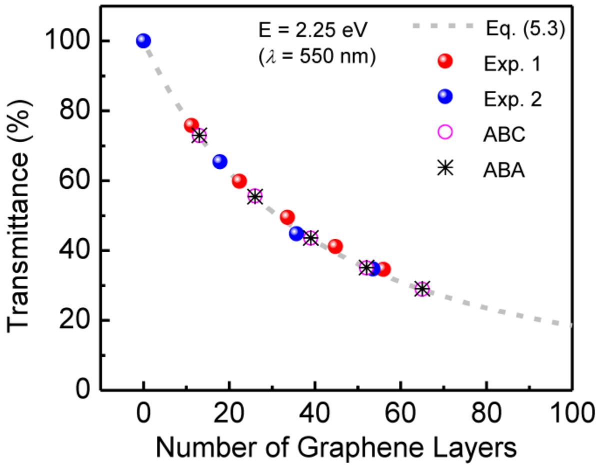

Figure 5.1: Optical transmittance of CVD multilayer graphene and simulation results. The red dots and blue dots are the experimental data points from multi-stacking. The gray dashed line indicate theoretical curve from Eq. (5.3). The magenta hollow circles and black stars indicate simulation data from ABC and ABA stacked multilayer graphene films, respectively.

In Fig. 5.1, we plot the numerical results of the optical transmittance of multilayer graphene as a function of the layer number by using the Kubo formula Eq. (5.4). We consider both ABA and ABC stacking sequence. The interlayer hopping parameters between the atomic sites in two nearest layers are set to be $t_1 = 0.12t$, $t_3 = 0.1t$, and $t_4 = -0.04t$ [10, 108]. For incident energy $E = 2.25$ eV ($\lambda = 550$ nm), the absorption of the light is the same for both ABA- and ABC-stacked multilayer graphene stacking sequence. This is due to the fact that interlayer hoppings mainly affect the band strcuture below the energy of t_1 and around the van Hove singularities [117]. Furthermore, the numerical results match the analytic approximation expressed in Eq. (5.3), and one can therefore estimate the layer number by measuring the optical transmittance and fit the results to Eq. (5.3) by using the optical conductivity of single layer graphene at 550nm wavelength.

5.3 Experimental section

In order to study the optical transmittance experimentally, large-area graphene films were synthesized through chemical vapor deposition (CVD). Monolayer graphene and multilayer graphene films were achieved with copper [24] and nickel [32] catalysts, respectively. The monolayer and multilayer graphene films were transferred onto a glass substrate with polymethyl methacrylate (PMMA), followed by etching away the metal catalyst, soaking in deionized (DI) water, releasing the graphene on a transparent substrate and solving the PMMA with acetone [24]. The transmittance of monolayer graphene was recorded using a Shimazdu ultraviolet–visible spectrometer (UV-3600). The light adsorption of glass substrate was subtracted for all the measurements. The monolayer CVD graphene shows a transmittance of 97.4% at normal incidence for 550 nm wavelength light as shown in Fig. 5.2. This value is slightly lower than 97.7%, which was previously attributed to the polymer residue [24]. However, it is clear that the experimental results of the monolayer coincide well with our numerical calculations in the range from 550 nm to 800 nm as shown in Fig. 5.2. Both from the simulations as well as from the tranmittance measurements on the monolayer graphene, we determine the value of $f(\omega)$ to be equal to 1.13 at 550 nm wavelength. As a comparison, the experimental data by Nair *et al.* [20] are plotted in blue hollow circles. These data match slightly less well to our tight-binding simulation. The deviations for $\lambda < 500$ nm can not be reproduced from our numerical simulations by considering small amout of disorder such as carbon vacancies or hydrogen adatoms (data not shown), but might be originated from the excitonic effect which is beyond our phenomenological consideration with a reduced hopping amplitude.

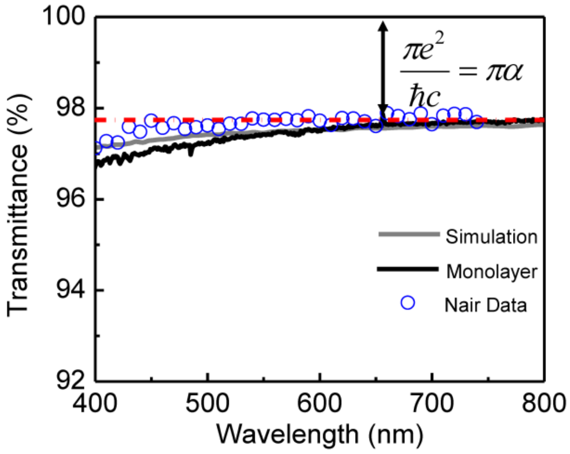

Figure 5.2: Optical transmittance of CVD monolayer graphene (black line) and simulation results (gray line). The blue open circles are the experiment data points from Nair *et al.* [20]. The red dash dot line indicates the light absorption $\pi\alpha$ of monolayer graphene predicted by Dirac cone approximation.

In order to verify the dependence of the optical transmittance of multilayer graphene layers, two sets of multilayer CVD graphene films were grown on a nickel coated wafer. The numbers of layers in the two sets are determined to be 11.2 and 17.8 by using Eq. (5.3), with $f(\omega) = 1.13$. The multilayer graphene films are polycrystalline with an irregular number of layers, however with uniform optical transparency on a macroscopic scale. These two sets were stacked upon themselves to get multilayers consisting of n times 11.2 and n times 17.8 layers, where n is the number of transfers. The transmittance curves of each of these stacks with λ ranging from 400 nm to 800 nm are presented in Fig. 5.3. The numbers in the figures indicate the optical transmittance at 550 nm incident light. We extracted the experimental data at 550 nm (Fig. 5.1) from multi-stacked graphene films in Fig. 5.3. In Fig. 5.1, the red dots represent the stacks fabricated by stacking the 11.2-layers sample, and the blue dots represent the stacks originating from the 17.8-layers sample. The experimental data points coincide very well with Eq. (5.3) as well as our numerical simulations.

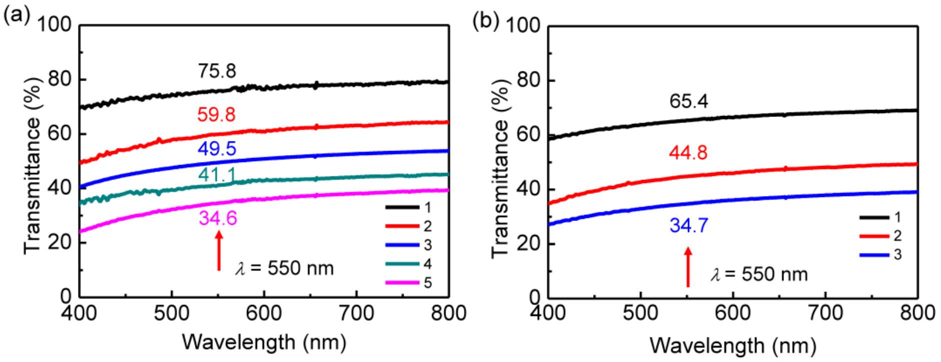

Figure 5.3: Optical transmittance of graphene films with multi-times transfer in two sets with incident light wavelength ranging from 400 nm to 800 nm. (a) The number of layers is determined to be 11.2. (b) The number of layers is determined to be 17.8. The data in the figures indicate the optical transmittance with incident 550 nm visible light.

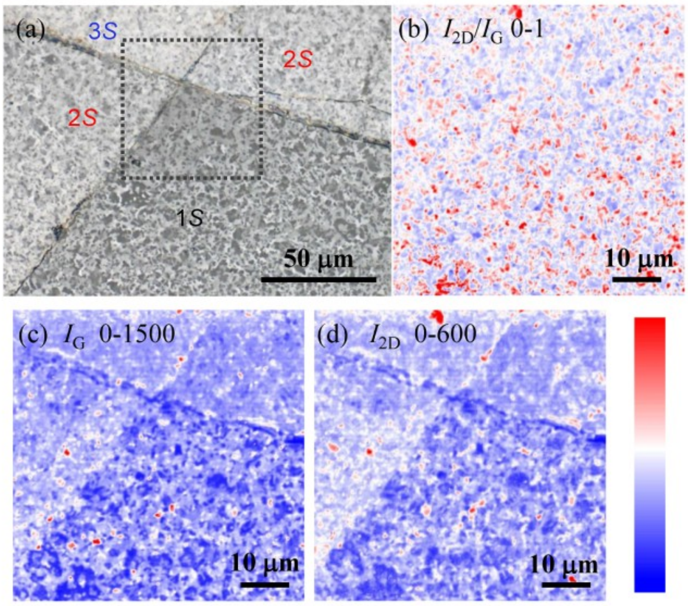

Figure 5.4: (a) Optical microscope image of multilayer layer graphene films transferred onto glass substrate. 1*S*, 2*S*, and 3*S* are corresponding to 1-, 2-, and 3-times stacking regions. (b) 2*D* and *G* peak Raman intensity ratio in the overlap multi-stacked region indicated by dotted square in panel (a). (c), (d) Raman intensities of *G* and 2*D* peak in the same region as in panel (b).

Raman Spectroscopy has been used to determine the number of layers in multilayer graphene consisting of a few layers [103]. The boundary region with 3-times stacking for 11.2-layers graphene films is presented in Fig. 5.4. The clear step edges for different times stacking can be distinguished in the corresponding region of the optical image as shown in Fig. 5.4a. We find that the intensities of the Raman *G* peak and 2*D* peak increase with stacking graphene films. However, the increase of intensity is no longer distinguishable between 2-times stacking and 3-times stacking. Intensity ratio between *G* mode and 2*D* mode has been a fingerprint to indentify the number of graphene layers [103]. In contrast, it does not provide clear information for our multi-stacking samples as shown in Fig. 5.4b. Raman spectra data for one time transfer and 5-times stacking are presented in Fig. 5.5. With number of graphene layers increases, the thickness becomes more uniform. However, no conclusive differences are observed due to the thicker graphene layers in our experiment, which clearly shows the limitation of Raman spectroscopy to determine the number of graphene layers over 9 [118].

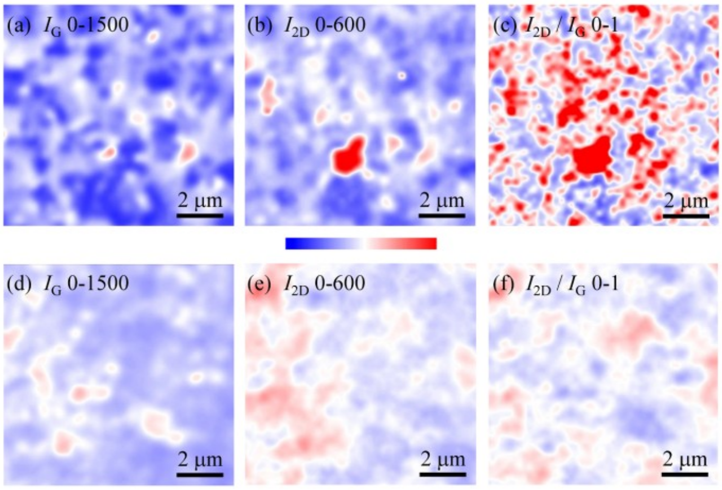

Figure 5.5: (a), (b), (c) Raman intensities and intensity ratio of *G* and 2*D* peak with one time transfer of 11.2-layers graphene films. (d), (e), (f) Raman intensities and intensity ratio of *G* and 2*D* peak after five times stacking.

5.4 Conclusion

In conclusion, our numerical and experimental studies of the optical transmittance in multilayer graphene films show that the nonlinear function $T = (1 + 1.13\pi\alpha N/2)^{-2}$ gives a good description of the light transmittance through multilayer graphene in the visible light range. It provides a simple way to determine the number of graphene layers by the measurement of the light transmittance. It is more reliable than the commonly used method Raman spectroscopy, and can be applied to other 2D materials with weak van der Waals interlayer interaction.

5.5 Acknowledgement

We acknowledge the financial support from the Delft Energy Initiative Fund, the Young Wild Idea Grant of the Delft Centre for Materials (DCMat), and the Netherlands National Computing Facilities Foundation (NCF). This work is part of the research program of the Foundation for Fundamental Research on Matter (FOM), which is part of the Netherlands Organisation for Scientific Research (NWO).

CHAPTER 6

Graphene based piezoresistive pressure sensor

Shou-En Zhu, Murali Krishna Ghatkesar, Chao Zhang, and G. C. A. M. Janssen

(Published in Appl. Phys. Lett. 102, 161904 (2013))

We present a pressure sensor based on the piezoresistive effect of graphene. The sensor is a 100 nm thick, 280 μm wide square silicon nitride membrane with graphene meander patterns located on the maximum strain area. The multilayer, polycrystalline graphene was obtained by chemical vapor deposition. Strain in graphene was generated by applying differential pressure across the membrane. Finite element simulation was used to analyze the strain distribution. By performing electromechanical measurements, we obtained a gauge factor of ~3.2 for graphene, and a dynamic range from 0 mbar to 700 mbar for the pressure sensor.

6.1 Introduction

Graphene, a monoatomic thin sp^2 bonded honeycomb carbon film, is the most robust material known. It shows novel optical, electrical, mechanical properties. Since the discovery of graphene in 2004 [3], an enormous amount of effort has been invested in order to realize application of graphene in prototype products such as flexible touch screens [24], high frequency transistors [119], and ultra-fast photodetectors [120]. One of the promising fields for graphene application is micro electro mechanical systems (MEMS), thanks to the extreme stiffness of graphene, with Young’s modulus of 1 TPa [9], excellent electrical conductivity compared to any other nano materials [14], super flexibility and stretchability up to 20% [32]. Furthermore, the resistivity of graphene varies linearly with strain [32, 121]. This piezoresistive effect is also observed in thin metal films and semiconductor films. The piezoresistive effect in those materials has been widely used in the MEMS smart sensor field, including strain gauges, cantilever force sensors, accelerometers, inertial sensors, and pressure sensors [122]. By providing an easy and direct transduction, the piezoresistive effect of graphene can be used to connect the mechanical and the electrical domains. At present various strain sensors based on graphene have been developed [32, 121, 123-126]. However, to our knowledge, the most important step for piezoresistive graphene, monolithic integration in silicon based MEMS, has not yet been reported.

6.2 Strain and displacement of pressure sensor

In this chapter, we present a graphene based piezoresistive pressure sensor based on standard semiconductor processes. A silicon nitride (SiN_x) suspended membrane was used as the structural element in this pressure sensor. The mechanical properties of the SiN_x membrane were measured by bulge testing. From the measurement of the center deflection as a function of the applied pressure, the stress-strain relation of the material can be obtained [127-129]. The schematic of a membrane under test is shown in Fig. 6.1a. When a differential pressure is applied, the force is uniformly distributed on top of the window, and the membrane undergoes deflection that is about two orders of magnitude larger than the membrane thickness. As illustrated in the Fig. 6.1b, the membrane deforms into a concave shape under differential pressure. The three dimensional (3D) surface profile of the membrane was mapped by the white light interferometer (WYKO NT3300 Optical Profiler). During the experiment, differential pressure ranging from 0 to 700 mbar in steps of 50 mbar was applied across the membrane, while the out of plane deflection profile of the membrane was recorded (see Fig. 6.1c). The maximum out-of-plane deflections δ were fitted with respect to differential pressure P by using the analytical Eq. (6.1) [128-130]:

$$P = \frac{B_1 t \sigma_o}{(a/2)^2}\delta + \frac{B_2 f(\nu) t E}{(a/2)^4 (1-\nu)}\delta^3 \tag{6.1}$$

Where B_1, B_2 are dimensionless constants, σ_o is the initial stress in the membrane, a is the side-length of the membrane, ν is Poisson Ratio, $f(\nu)$ is geometry function and the value was set to be: 1-0.271 ν in this report [130], t is the thickness of membrane, *E* is Young's Modulus. The parameters used are listed in Table 6.1. In order to map the strain of the SiN_x membrane, a simulation model was created using the finite element package (COMSOL Multiphysics), where the fixed square support boundary condition was applied to the four edges. The maximum tensile strain of ~0.25% occurs at the middle of each edge (normal strain perpendicular to the edge) as illustrated in Fig. 6.2b, the differential pressure in the model was set as 600 mbar. So, the locations with high tensile strain were selected for the placement of piezoresistive sensors.

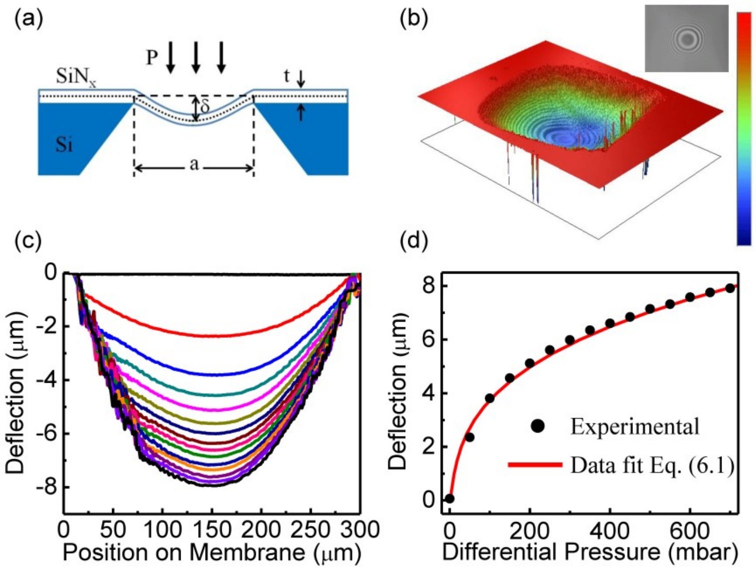

Figure 6.1: (a) Schematic of suspended silicon nitride diaphragm under the applied differential pressure (The drawing is not to scale). (b) 3D deformation image of the SiN$_x$ membrane under differential pressure created by WYKO NT3300 Optical Profiler (scale red to blue: 0 to -6 μm). Inset shows typical optical interference fringes from the white light profilometer. (c) Deflection profile of the diaphragm under the differential pressure from 0 mbar to 700 mbar (50 mbar per step). (d) Deflection versus differential pressure of 100 nm SiN$_x$ membrane. Experimental data were fitted by the red line Eq. (6.1) to estimate plane-strain elastic modulus presented in Table 6.1.

Table 6.1: Properties of square SiN$_x$ membrane.

LPCVD SiN$_x$ membrane	Value	Refs.
Thickness (nm)	100	
Length (μm)	280	
Residue stress (MPa)	50	
Constant B1	3.45	[130]
Constant B2	1.994	[130]
Poisson's ratio	0.22	[131]
Young's Modulus (GPa)	200	[131]

6.3 Resistance of graphene and Wheatstone bridge

The strain of graphene was assumed to be the same as the strain on top of the SiN_x membrane. In order to effectively increase the length of the resistor and the amount of total resistance, graphene was cut in a meandering pattern by e-beam lithography within the high strain area as shown in Fig. 6.2a. Resistance changes were measured using a Wheatstone bridge circuit. The Wheatstone bridge consists of four resistors connected in a loop. An input voltage of 2.5 V is applied across junctions of two parallel circuits as shown in inset of Fig. 6.2c. Voltage drop across the resistors forms the output. The graphene piezoresistor R_g that varies with strain was represented by $R_g=R+\Delta R$, and R was measured to be 74.3 kΩ (Fig. 6.2d). The other resistors R_1, R_2 and R_3 resistors were turned to be identical in value with the unstrained graphene resistor R, and located on a rigid Printed Circuit Board (PCB). The output voltage is linearly proportional the input voltage V_{in} (2.5 V), according to the Eq. (6.2):

$$V_{out} = V_{in}\left(\frac{R_2}{R_1+R_2} - \frac{R_3}{R_3+R_g}\right) = \frac{1}{2}V_{in}\left(\frac{\Delta R}{2R+\Delta R}\right) \tag{6.2}$$

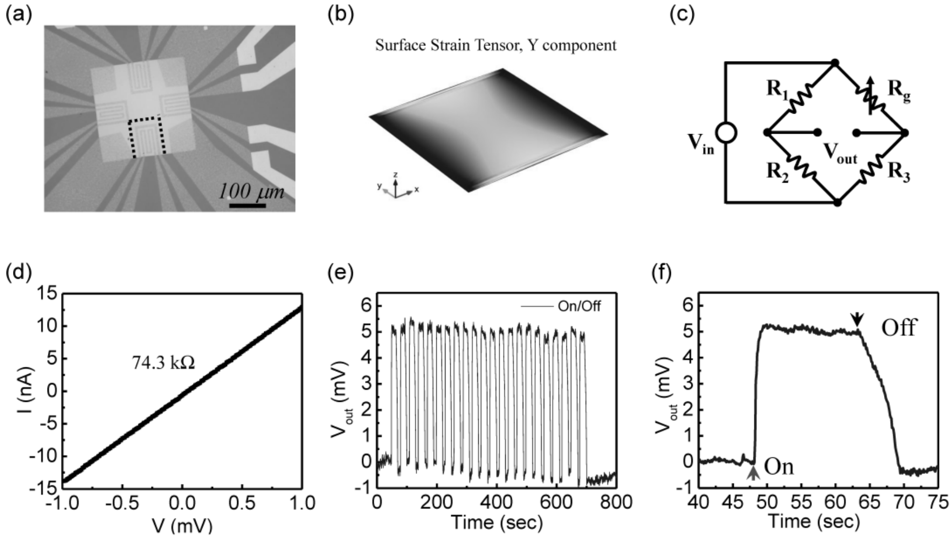

Figure 6.2: (a) Optical microscope image of graphene piezoresistors on silicon nitride square membrane (The dotted lines highlight the device used for the measurement). (b) Y

component of surface strain tensor, the entire surface shows tensile strain under differential pressure. The maximum strain occurs at the center of each edge (green: ~0.25 % strain, blue ~0 % strain). The X component of the tensor shows same behavior as Y component. (c) Schematic of Wheatstone bridge measurement for the change of graphene resistance. (d) Resistance measurement of graphene meander. (e) Output voltage versus time during cycling test with switching ON/OFF 600 mbar differential pressure. (f) One typical cycle in (e) with 15 sec ON 15 sec OFF under 600 mbar differential pressure (ON/OFF indicates the switching of the valve for vacuum).

6.4 Piezoresistivity of graphene

In our measurement, the measured resistance variation of graphene was less than 1%. The reversible performance of the graphene piezoresistor was observed by switching the pressure in 22 cycles of ON/OFF test (Fig. 6.2e), (which shows little degradation). The detail of each cycle is illustrated in Fig. 6.2f. Each switching cycle was performed by turning the vacuum pump on/off with fixed 600 mbar differential pressure. The ~ 5 mV transition, which is equal to 0.4% of resistance change, was reached in 0.9 sec. While turning off the pump, the strain was fully relaxed after 5.6 sec due to the slow venting of the gas line. Measurements were also made at different differential pressures across the membrane as shown in Fig 6.3a. The output intensity increased in distinct steps as the tensile strain applied on graphene piezoresitor was increased. These well-defined steps show the immediate response of the piezoresistive effect to the deformation of membrane. At 247 sec, the valve of the gas pump was closed. After slow venting of 15 sec, the output signal returned to 0 mV. This reverse (restore) time was determined by the response of the venting speed and the manual control when adjusting the differential pressure, and so the actual response time is anticipated to be faster. The ability to monitor the step of pressure demonstrates the accuracy of graphene piezoresistive effect for application of the pressure sensor. The output voltages as function of applied differential pressure were also plotted in Fig. 6.3b. It is clear that a good linearity was observed up to 500 mbar, and the sensor sensitivity ~8.5 mV/bar was obtained by fitting the slope. The standard deviation was less than 0.13 mV, which is ~2.2 % with respect to its dynamic range, i.e. 15 mbar at 700 mbar full scale. The pressure sensor working range, accuracy and sensitivity can be further increased by changing the membrane thickness, optimizing graphene location and sensing wire pattern, and designing low noise electronics suitable for graphene. Finally, the gauge factor G of the graphene piezoresistor can be estimated from the change in resistance related to the applied strain. $G = \frac{\Delta R/R}{\Delta L/L} = \frac{\Delta R/R}{\varepsilon} = \sim 3.2$, which is in agreement with former reports, e.g. exfoliated graphene ~1.9 with ~3% strain [125]; CVD graphene ~6.1 with 1% strain [121]; and graphene ripples ~2 with an applied strain up to 30% [124]. This demonstrates the feasibility of a sensitive pressure sensor comparable to the metal based strain gauge.

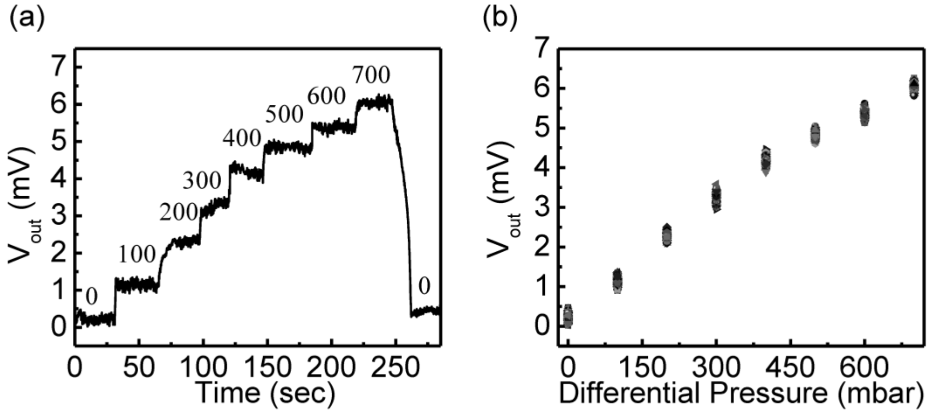

Figure 6.3: (a) Dynamic output voltage versus time under differential pressure with step increase from 100 mbar to 700 mbar (100 mbar per step). (b) Output voltage as function of the differential pressure.

6.5 Conclusion

In conclusion, a graphene based piezoresistive pressure sensor was developed by integrating graphene resistors on a SiN_x membrane. The characteristics of the graphene piezoresistive effect and the sensitivity as function of applied differential pressure demonstrated the high performance of graphene for pressure sensor application. This semiconductor compatible and controllable fabrication processes can pave a route for graphene based piezoresistive MEMS devices.

6.6 Acknowledgement

We acknowledge V. E. Calado for e-beam lithography, R. Luttjeboer, J. van Driel, M. Langelaar, H. Jansen, P. van Holst for discussions and technical support. We acknowledge the financial support from the Young Wild Idea Grant of the Delft Centre for Materials. This work is part of the research program of the Foundation for Fundamental Research on Matter (FOM), which is part of the Netherlands Organisation for Scientific Research (NWO).

CHAPTER 7

Infrared nano-imaging of plasmons in graphene

Shou-En Zhu, Zhe Fei, Jhih-Sheng Wu, Siyuan Dai, Martin Wagner,
Alexander McLeod, M.D. Goldflam, Mengkun Liu, Kirk Post,
Michael Fogler, D.N. Basov, G.C.A.M. Janssen

Surface plasmons, collective oscillation of charges on the surface of metals or semiconductors, have been harnessed to confine and manipulate electromagnetic energy at the nanometer length scale. In particular, surface plasmons in graphene are promising for optoelectronic applications in a wide frequency range from terahertz to infrared (IR). However, the plasmon damping in previously reported graphene/SiO_2 devices is much higher than theoretical predictions. Here, we carry out infrared nano-imaging measurements of the surface and edge plasmons in chemical-vapor-deposited graphene single crystals on aluminum oxide (Al_2O_3) substrates. We demonstrate that the plasmon damping in graphene on Al_2O_3 is much smaller than that on SiO_2, where the effects due to the optical phonons are absent. Moreover, we observe edge plasmons, which are localized at the graphene edges. These plasmons show a higher confinement and longer propagation length as compared to surface modes. A possible mechanism for the observation of the edge plasmons is proposed.

7.1 Introduction

Surface plasmon polaritons are highly confined electromagnetic waves that propagate at the interface of a metal and dielectric. These highly confined waves are promising for future applications in plasmonic sensing, solar energy harvesting, field enhanced spectroscopy and nanoscale information transfer [132, 133]. However, the strong confinement also leads to a higher energy loss, which is one of the major obstacles to infrared applications. Graphene, one atomic layer of carbon atoms, has been proven to be a promising plasmonic material that surpasses noble metals in many important aspects[134]. The limiting aspect of current graphene plasmonic devices is the plasmon damping that originates from electron-electron, electron-impurity, and electron-phonon scattering [135, 136]. The intrinsic lifetime of plasmons has been predicted to be 20-120 ps in the mid-infrared (MIR) range [135]. However, previous studies show that plasmons in exfoliated graphene on SiO_2 substrates[137] and epitaxial graphene on SiC substrates[138, 139] have much shorter lifetimes, typically ~300 fs [137]. SiO_2 is known to be an imperfect substrate with impurities, dangling bonds and broad range mid-infrared (MIR) optical phonons (800 – 1200 cm^{-1}). Epitaxial graphene on SiC has a small electronic mobility, typically less than 1000 cm^{-2}/Vs [139]. All these factors strongly impede plasmon propagation and prevent the realization of devices which reach the theoretically predicted upper limit on lifetime.

In this work, in order to improve the plasmonic performance in graphene, we fabricated graphene single crystals using chemical vapor deposition (CVD). The crystals were then transferred to Al_2O_3 substrates grown by atomic layer deposition (ALD). As discussed in detail below, the optical phonons of the Al_2O_3 substrates are at frequencies less than 1000 cm^{-1}, allowing for a wide range of MIR frequency region that is free from phonons. By combining atomic force microscopy (AFM), near-field microscopy, Fourier-transform infrared spectroscopy (FTIR), and numerical modeling, we systematically studied plasmons in the graphene/Al_2O_3 system. We found that the plasmon damping rate in our device is ~0.03, a factor of 4 higher than previous studies [137]. Furthermore, edge plasmons in the graphene/Al_2O_3 system are for the first time imaged with ~20% shorter wavelength compared to the surface plasmons.

7.2 Near field optical measurement

Real space infrared (IR) nano-imaging experiments were carried out at UCSD using a scattering-type scanning near-field optical microscope (s-SNOM) as depicted in Fig. 7.1a [137, 139]. Here, a metalized AFM tip is illuminated by a p-polarized mid-infrared (MIR) beam thus generating strong near fields with a wide range of in-plane momenta *q* underneath the tip [140]. These momenta, which can exceed the far-field wavevector by two orders of magnitude, allow for energy transfer and momentum matching between the incident photons and excited plasmons [141]. The backscattered MIR signal recorded simultaneously with the AFM topography is a direct measure of the electric field underneath the AFM tip.

Our samples are arrays of graphene nanoribbons and nanodisks fabricated at Delft on Al_2O_3 substrates. As shown in the AFM image (Fig. 7.1b), these nanoribbons have various ribbon widths from 100 to 450 nm. The representative near-field images are shown in Figs. 7.1c–f, where we plot the third harmonic near-field amplitude normalized to that of the bare Al_2O_3 substrate, $\mathrm{s}(\omega) = \mathrm{s}_3(\omega)/\mathrm{s}_3^{Al_2O_3}(\omega)$. As shown in these images, there are bright fringes formed inside the ribbons that are parallel to the edges (white dashed lines). According to previous studies, these fringes originate from interference between tip-launched and edge-reflected plasmons causing periodic field variation beneath the AFM tip [137, 139]. The principal fringes (closest to the edges) show highest amplitude while subsequent inner fringes are much weaker. Moreover, the number of fringes confined within the nanoribbons decreases with ribbon width *W*.

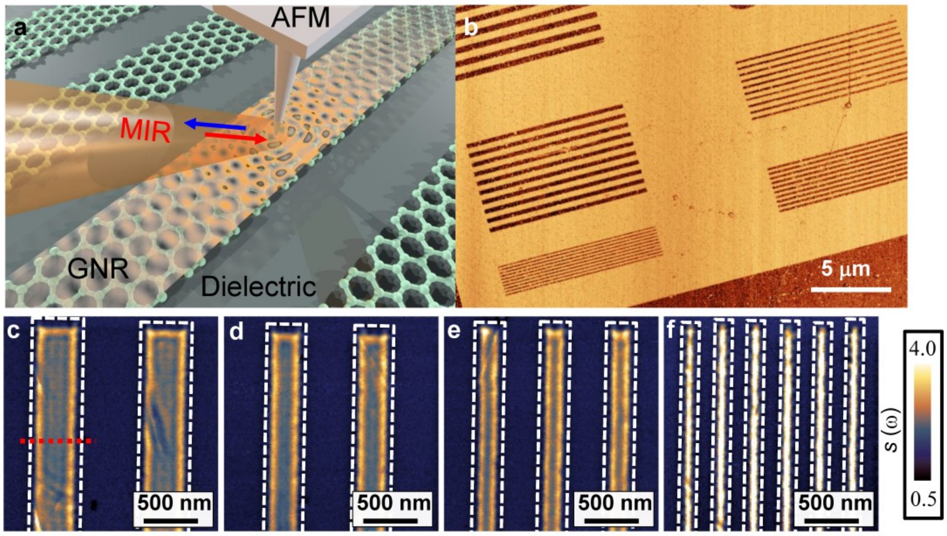

Figure 7.1: Infrared nano-imaging of graphene nanoribbons. (a) Schematic of a MIR nano-imaging experiment. A metalized AFM tip is illuminated with MIR light (red arrow) launching plasmons waves inside a graphene nanoribbon (GNR) on the Al_2O_3 substrate. The back-scattered signal (blue arrow) from the tip is recorded in the far field. (b) The AFM phase image of GNR arrays with various widths. (c-f) Images of normalized amplitude $s(\omega)$ at incident MIR frequency $\omega = 1184.4$ cm^{-1} of GNR with width from 450 to 100 nm, respectively. White dashed lines mark the graphene edges. All data were acquired at ambient conditions.

In order to explore the frequency dependence of these fringe patterns, we performed infrared nano-imaging with both tunable monochromic lasers and broadband lasers. In Fig. 7.2a, we show the $s(\omega)$ profiles perpendicular to the vertical edges of a 450 nm nanoribbon at several discrete frequencies. Distinct features can be observed in these profiles. Firstly, all the plasmon fringes are symmetrically located within the interior of the graphene nanoribbon, indicating that the plasmons reflectors are the edges of graphene. In addition, with decreasing ω_{MIR} , the peak positions of the principal fringes move towards the center and their widths increases. As a result, the number of plasmons fringes is reduced from 5 to 1. Moreover, $s(\omega)$ of the principle fringes increases with decreasing ω_{MIR} and reaches its maximum value at ~1065 cm^{-1}. The principal fringes start to merge and form one dome at the ribbon center with the decrease of the incident ω_{MIR}

towards 935 cm^{-1}. A strong decrease in $s(\omega)$ is observed as ω_{MIR} further approaches 890 cm^{-1}. Interestingly, we found two small shoulder peaks closed to the edges as shown by red arrows and the relative intensities decrease as ω_{MIR} increase from 890 cm^{-1} to 1310 cm^{-1} as shown in Fig. 7.2a. The detail of these modes will be discussed in the later part of our work.

Broad-band nano-FTIR was further performed, which is capable of capturing near field signal over the effective ω_{MIR} spectral width ~400 cm^{-1} simultaneously [142, 143]. Three independent line scans at center frequency of 1000, 1200, and 1300 cm^{-1} were recorded and stitched to form one spectrum map (Fig. 7.2b). The spectra from all pixels along the graphene nanoribbon line scans were combined and form a 2D map as shown in Fig. 7.2b. In the plot, we observed the position and width of principle fringes systematically vary with frequency ω_{MIR}. The quantitative relation between $s(\omega)$ profile, the damping rate of plasmons γ_{p} ($\gamma_{\mathrm{p}} = q_2/q_1$, $q=q_1+iq_2$), the plasmon frequency (ω) – momentum (q) dispersion, and the plasmon coupling with substrate phonons can be established by numerical modeling of the near-field response in graphene/Al_2O_3 [137, 140]. The complete map of $s(\omega)$ over a broad-band spectrum ranging from 950 to 1450 cm^{-1} by modeling is displayed in Fig. 7.2c. The ribbon edges are delineated by two white dashed lines. The white dots mark the positions of $s(\omega)$ maxima. The shift and splitting of fringes with increasing ω_{MIR} can be clearly seen in the map, implying the decrease of plasmons wavelength λ_{p} with decreasing λ_{MIR}. The peak positions of fringes match quantitatively the experimental observation, which confirm the propagation, reflection and interference behavior of tip excited plasmons in graphene [137].

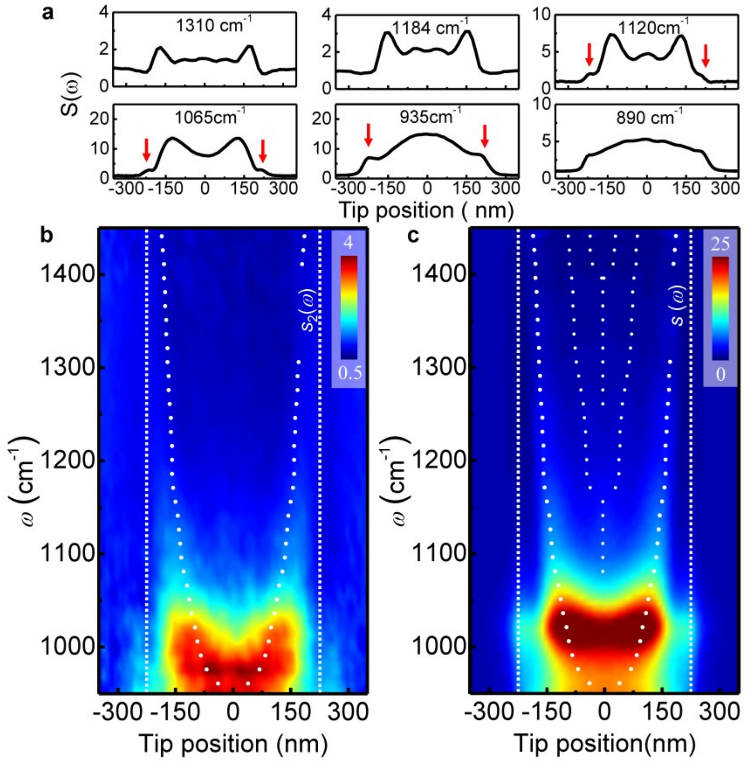

Figure 7.2: The frequency-dependence of the plasmon fringes in graphene nanoribbons. (a) Line profile of normalized amplitude $s(\omega)$ at discrete MIR frequency along the red dotted line in Fig. 7.1c. (b) Nano-FTIR spectra recorded along the red dotted line in Fig. 7.1c. White dashed lines in Fig. 7.2 b and c indicate the edge of GNR. (c) Diagram of numerical modeling results of $s(\omega)$ along 450 nm GNR at broad-band MIR frequency ranging from 850 to 1450 cm^{-1}. White dots indicate the positions of fringe maxima at each frequency. The position of principle fringes from panel c was marked in panel b as a guide to the eye.

7.3 Plasmon damping rate

The plasmon damping rate γ_p versus ω_{MIR} extracted from fitting of the monochromic dataset (Fig. 7.2a) are plotted in Fig. 7.3a. One can see that γ_p reaches its minimum value of 0.03 at ~1184 cm^{-1} and then increases exponentially when ω_{MIR} approaches 850 cm^{-1}. To understand the underlying physics, broad-band nano-FTIR measurements $s_2(\omega)$ (the signal from the second harmonics demodulation) were carried out on Al_2O_3 substrate with and without graphene. As shown in Fig. 7.3b, there is a strong near-field resonance at 843 cm^{-1} for the bare Al_2O_3 substrate (black curve in Fig. 7.3b). The observed resonance originates from the optical phonon of Al_2O_3. Moreover, graphene significantly enhances the resonance and causes a slight blue shift (~7 cm^{-1}). According to previous studies [140], these effects can be attributed to the hybridization of Dirac plasmons in graphene and the localized surface optical phonon mode in Al_2O_3. The hybridization and localization result in and increased damping rate and the emergence of a non-propagating plasmon-phonon mode over a band width of ~100 cm^{-1} (Figs. 2b, 3a, and 3b). The key figure of merit for plasmons is the lifetime (average collision time) $\tau = 1/(\gamma_p \cdot \omega)$. Here, plasmon lifetime was calculated to be 940 fs at ~1184 cm^{-1}, which is close to the highest value ever measured in graphene[137, 144]. In comparison, the SiO_2 surface phonon modes[140] at 806 cm^{-1} and 1168 cm^{-1} lead to strong interaction with the plasmon branch located ~900 cm^{-1}, resulting in the stronger damping observed in previous experiments [137, 139].

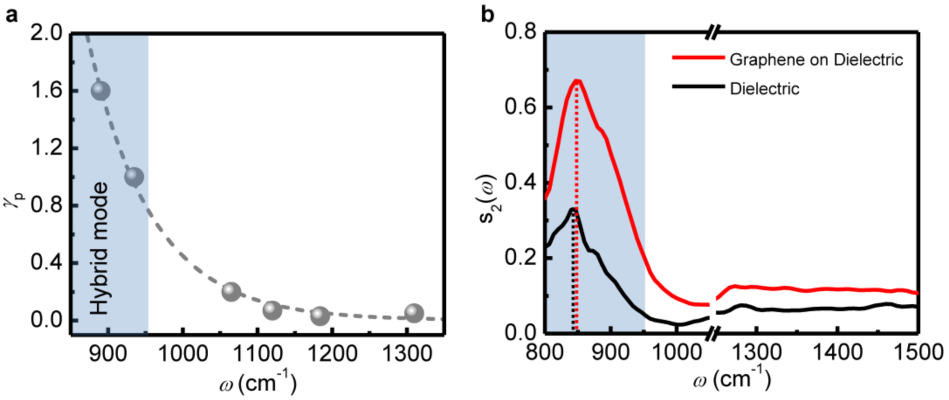

Figure 7.3: The dispersion of graphene plasmons and the parameters. **a**, Numerical modeling fitting parameter of damping rate at discrete MIR frequency. The dots indicate the fitting damping rate at certain frequencies. Gray dashed line indicates the exponential curve. Shade area (light blue) highlights the plasmons-phonon hybridization frequency range. **b**, Nano-FTIR spectra of bare Al_2O_3 substrate and large scale graphene on Al_2O_3.

7.4 Plasmon edge mode and wavelength

In order to eliminate the interactions between reflected plasmons and further evaluate the wavelength of plasmons λ_p with incident ω_{MIR} , a graphene disk-like pattern with diameter ~2.1 micron was fabricated from the same graphene crystal as the ribbon. Standing oscillations with a period of $\lambda_p/2$ from graphene edge are shown in Fig. 7.4a, where λ_p is the plasmon wavelength [137]. Fig. 7.4b shows a zoomed in region in Fig. 7.4a, where the top left corner is the center of the disk. The line profiles of standing wave from the edge of graphene at discrete ω_{MIR} are plotted in Fig. 7.4d. An increase of λ_p can be observed with decreasing incident ω_{MIR} as shown in Fig. 7.4b and c. The momenta of the plasmons $q(\omega)$ at discrete incident ω_{MIR} are plotted as hollow circles in Fig. 7.5, where the experimental data points agree very well with the calculation.

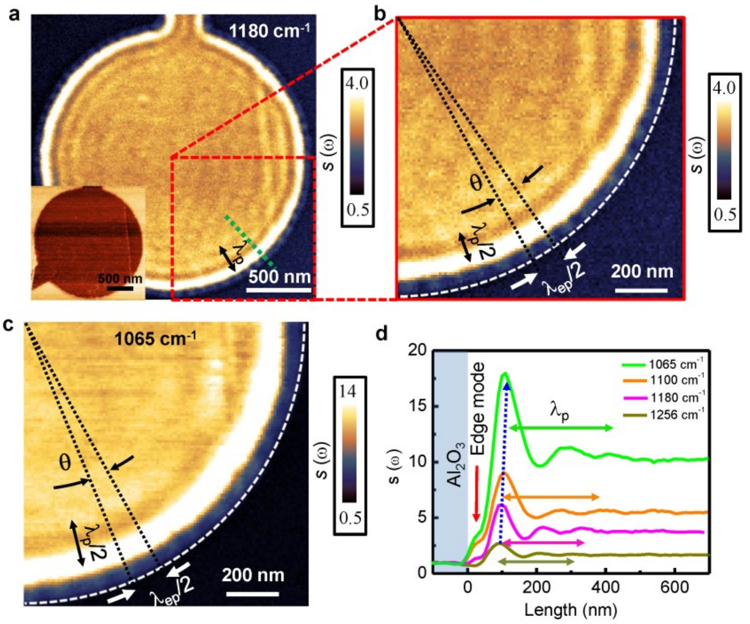

Figure 7.4: Nano-imaging of surface and edge plasmons modes in graphene micro-disks. **a**, Image of normalized amplitude $s(\omega)$ at 1180 cm^{-1} for graphene micron disk-like pattern on Al_2O_3 substrate. Inset: AFM phase image simultaneously recorded in corresponding nano-imaging area. **b**, Zoom in region of red dashed square in Fig. 7.4a. The distance between circular fringes, and the arc length along the circumference are used to determine the wavelength of surface mode and edge mode of plasmons, respectively. White dashed line indicates the edge of graphene. Black arrow specifies the method to determine the wavelength of surface plasmons. **c**, Image of normalized amplitude $s(\omega)$ at 1065 cm^{-1} in the same region as in Fig. 7.4b. **d**, Line profiles of the normalized amplitude $s(\omega)$ along the

radial direction (green dotted line in Fig. 7.4a) at discrete MIR frequency. Shade area (light blue) indicates bare Al_2O_3 substrate region. Red arrow indicates position of edge mode of plasmons.

The dispersion diagram of surface excitation at the Graphene/Al_2O_3 interface is given in Fig. 7.5, where we plot the calculated imaginary part of the reflection coefficient $r_p(q, \omega)$. According to previous studies, the maxima of $Im(r_p)$ determines the surface modes including graphene plasmons, substrate phonons and their hybrid modes[140]. The graphene chemical potential used in our calculation was set to be $\mu = 2800\ cm^{-1}$ (Fermi energy $E_F = 0.35$ eV), which gave the best fit for our experiments. The intrinsic optical phonon mode of graphene at 1595.4 cm^{-1} measured from Raman Spectroscopy was highlighted as white dashed line. It is clear that dispersion curve of plasmons is away from the phonon modes, and high quality CVD graphene (the absent of Raman D peak), further lead to low damping rate observed in our Graphene/Al_2O_3 system.

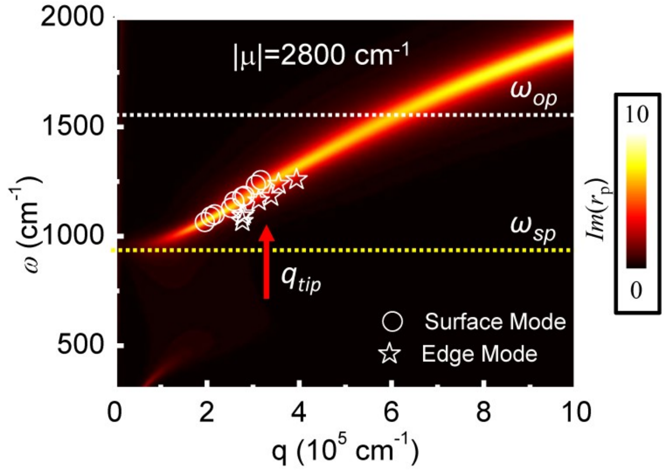

Figure 7.5: The dispersion of surface mode and edge mode of graphene plasmons. Imaginary part of the reflection coefficient $r_p(q, \omega)$ with chemical potentials $|\mu|=2800\ cm^{-1}$, and color scale is presented in the right. White dashed line marks the intrinsic optical phonon frequency obtained from Raman Spectrum. Yellow dashed line indicates the surface polar phonon from Al_2O_3 substrate. White hollow circles and stars indicate the experimental (q, ω) relation obtained from surface and edge mode of graphene plasmons, respectively.

Edge mode of graphene plasmons has been reported before to have a wavelength shorter compared to that of the surface mode[145-147]. We notice that there are periodic fringes distributed along the circular edges of graphene pattern. These modes are ~50 nm wide and locate along the edge of the graphene, and the intensity is ~20 % compared to that of the principle fringes discussed previously. The wavelengths λ_{ep} of these edge modes was calculated as $\lambda_{ep}=2\theta L$. Here, θ is central angle between consecutive fringes of edge modes, and the L is the radius of disk (~1.02 μm, count from the disk center to the middle of edge mode). To obtain a reliable arc length, we extract the $s(\omega)$ profile along the edge as shown in Fig. 7.6a and b. To determine accurately the wavelength of edge plasmons, we first performed Fourier transform (FFT) on the profile (Fig. 7.6c) and then calculate the wavelength by 2*pi/k_peak. The dispersion of these modes was plotted as hollow stars in Fig. 7.5. We found that this mode has ~20% shorter wavelength and follow the same propagating wave behavior as the surface plasmons mode [148]. Based on the collisionless approximation for the edge mode of graphene plasmons: $\omega_{edge}^{2}(q)=\omega_{p}^{2}(q)/\eta_{0}$, $\eta_{0}=1.217$ [147], the wavelength of edge mode of graphene plasmons is ~18% shorter than that of surface mode. From this feature, we can confirm that the mode close to the edge of graphene we observed as shown in Fig. 7.4b and c is the edge mode of graphene plasmons. Since the damping rate of edge mode is only related to the graphene optical conductivity, we expect the edge modes should have similar propagation length compared to the suface modes. A hypothetical multi-reflectors model is presented in Fig. 7.6d and e aiming to provide a preliminary explanation of the occurrence of the edge mode. Defects or sharp edges induced by oxygen plasma etching can act as reflectors for plasmons. Periodic fringes are measured due to the interference between tip excited plasmons and the reflected plasmons at the defects. Due to the resolution limit, we cannot extract the damping behavior in the edge modes. Further experiments are required to get the precise propagating length of the edge mode. These high confinement and low damping features may open a door for many graphene plasmonics applications.

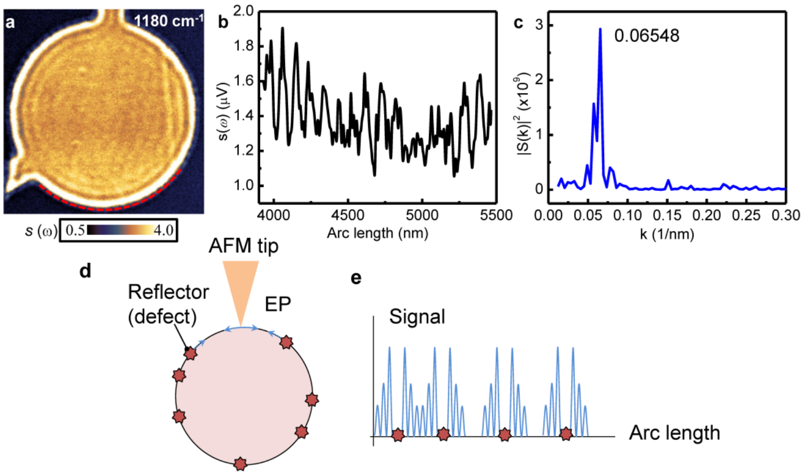

Figure 7.6 Profile and wavelength of edge mode of graphene plasmons. (a) Image of normalized amplitude $s(\omega)$ at 1180 cm^{-1} for graphene micron disk-like pattern. (b) Line profile of amplitude $s(\omega)$ along the edge indicated as red curve in Fig. 7.5a. (c) Fast Fourier transform (FFT) of the amplitude profile in Fig. 7.5b. (d-e) A model for the detection of the edge mode of graphene plasmons.

7.5 Conclusion

In conclusion, we have systematically studied the plasmons behavior in the graphene/Al_2O_3 system by nano-imaging experiments and numerical modeling. The dispersion of edge plasmons in graphene over broad-band infrared frequency range was confirmed for the time. Low damping rate of surface plasmons can be realized by using single crystal graphene and evading the dielectric phonon depression. The demonstration of edge mode at room temperature will further boost the promise of plasmonics applications in optoelectronics.

7.6 Acknowledgement

We acknowledge the financial support from the Young Wild Idea Grant of the Delft Centre for Materials and Delft Energy Initiative Fund. This work is part of the research program of the Foundation for Fundamental Research on Matter (FOM), which is part of the Netherlands Organisation for Scientific Research (NWO).

CHAPTER 8

Summary

8.1 Introduction

Experimental work on graphene started with the groundbreaking publication by Prof. Novoselov and Geim in 2004 [3]. In that publication the properties of graphene were heralded "*Graphene may be the best possible metal for metallic transistor applications… nontransistor applications of this atomically thin material ultimately may prove to be the most exciting.*" The award of Nobel Prize in 2010 further inspired the scientific communitiy and facilitated a large investment from the European Union (10 year research initiative project "European Graphene Flagship"). This swift development causes society to dream about practical future applications of graphene.

The status of an emerging technology from its discovery to consumer products can be positioned according to the technology life cycle curve proposed by Gartner Reseach (Fig. 8.1). A successful technology usually experiences the following five key phases: Technology trigger, peak of inflated expectations, trough of disillusionment, slope of enlightenment, and plateau of productivity. With this curve, it is possible to distinguish a technology hype from valorisation. The groundbreaking experiment in 2004 can be recognized as the starting point or graphene technology trigger. The award of the Nobel Physics Prize in 2010 and the granting of 10 years project "European Graphene Flasghip" would be definitely marked in the peak of inflated expectations for graphene technology. Numerous start-up companies are mushrooming from less than 5 in 2010 to over 50 in 2014. While the subject of graphene has been constantly exciting society, the actual development is still in its infancy. Most of the companies are currently focusing on supplying the raw material or production machines. The main driving forces so far are from the academic research and the R&D sector in industry. Graphene still lacks a killer application.

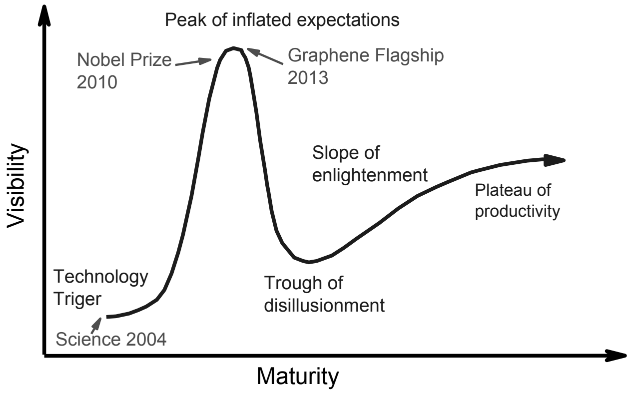

Figure 8.1: Life cycle of emerging technology. Five key phases are indicated in the horizontal ordinate, Technology trigger, peak of inflated expectations, trough of disillusionment, slope of enlightenment, and plateau of productivity. (Redraw based on the Hype Cycle of Gartner Research)

8.2 What does this thesis contribute to the development of a graphene technology

In this thesis, I have shown that the quality of synthetic graphene can be as high as mechanically exfoliated graphene if we can get rid of the wrinkles. Any defects, impurities and grain boundaries will induce scattering, preventing ballistic transport. The experiment described in chapter 4 was the first to demonstrate ballistic transport in synthetic graphene, and it will pave the way for the mass production of high quality monolayer graphene. In 2008, monolayer graphene was difficult to make and it was ranked as the most expensive material in the world. A piece of mechanically exfoliated monolayer graphene with size smaller than the diameter of a human hair will cost more than $1,000 from Graphene Research Ltd in Manchester [149]. Currently (2014), Monolayer graphene single crystals with size up to millimeters in diameter have already been routinely produced worldwide, and the price per cm^2 sample has dropped to less than $200.

In chapter 5 of this thesis, a parameterless equation was provided to calculate the number of graphene layers by measuring the transmittance of graphene films. The search for novel transparent electrode materials with good stability, high transparency and excellent conductivity is driven by the required trade-off between transparency and conductivity: Metals are very conductive but not transparent; plastics are quite transparent but not conductive. Graphene is a transparent and conductive material. However, the conductivity of monolayer graphene might not be sufficient for fabricating a highly conductive electrode. The dilemma is that the transmittance of a graphene film decreases as the number of layers increases. It therefore is of great importance to have a fast and reliable method to determine the number of layers in the fabrication and measurement of multilayer graphene. Having a simple relation to determine how many graphene layers can meet the transmittance requirement and provide good conductivity at the same time is a valuable tool.

I have also successfully demonstrated the integration of graphene into silicon chips, and the pressure sensor devices can potentially be produced in wafer scale. A sensitivity of ~8.5 mV/bar was obtained, and the standard deviation was less than 15 mbar at 700 mbar full scale. This chip scale integration of graphene devices is a key process to link the current semiconductor technology and the future applications of high quality graphene films. The further development of wafer scale automation transfer process is one of the directions to realize the valorisation of graphene.

In chapter 7 of this thesis, I have shown the potential application of graphene for optoelectronics devices. The speed of optoelectronics will outperform the current transistors especially in transmitting high-volume information on chip scale.

Although lots of technical issues are still waiting to be solved and the delivery of high quality and large quantity of graphene based products is still a key issue, tremendous progresses has been made in graphene research.

8. Summary

In the scope of 10-20 years, I believe that the price of large-scale monolayer graphene will drop below \$1/cm^2 comparable to the price of gate-oxide, which will enable graphene to enter potential markets, such as optoelectronics computing, flexible sensors and wearable devices, etc. There will be bright future for graphene technology.

Bibliography

1. Geim, A.K., *Nobel Lecture: Random walk to graphene.* Reviews of Modern Physics, 2011. **83**(3): p. 851-862.
2. Novoselov, K.S., *Nobel Lecture: Graphene: Materials in the Flatland.* Reviews of Modern Physics, 2011. **83**(3): p. 837-849.
3. Novoselov, K.S., et al., *Electric field effect in atomically thin carbon films.* Science, 2004. **306**(5696): p. 666-669.
4. Bardeen, J., *Research Leading to Point-Contact Transistor.* Science, 1957. **126**(3264): p. 105-113.
5. Boehm, H.P., et al., *Das Adsorptionsverhalten Sehr Dunner Kohlenstoff-Folien.* Zeitschrift Fur Anorganische Und Allgemeine Chemie, 1962. **316**(3-4): p. 119-127.
6. Ruess, G. and F. Vogt, **Hochstlamellarer Kohlenstoff Aus Graphitoxyhydroxyd - Uber Den Ort Der Aktiven Eigenschaften Am Kohlenstoffkristall.* Monatshefte Fur Chemie, 1948. **78**(3-4): p. 222-242.
7. Kelly, B.T., *Physics of graphite*1981, London ; Englewood, N.J.: Applied Science. x, 477 p.
8. Dresselhaus, M.S., G. Dresselhaus, and P.C. Eklund, *Science of fullerenes and carbon nanotubes*1996, San Diego: Academic Press. xviii, 965 p.
9. Lee, C., et al., *Measurement of the elastic properties and intrinsic strength of monolayer graphene.* Science, 2008. **321**(5887): p. 385-388.
10. Castro Neto, A.H., et al., *The electronic properties of graphene.* Reviews of Modern Physics, 2009. **81**(1): p. 109-162.
11. Katsnelson, M.I., *Graphene: carbon in two dimensions.* Materials Today, 2007. **10**(1-2): p. 20-27.
12. Castro Neto, A.H., F. Guinea, and N.M.R. Peres, *Drawing conclusions from graphene.* Physics World, 2006. **19**(11): p. 33-37.
13. Morozov, S.V., et al., *Giant intrinsic carrier mobilities in graphene and its bilayer.* Physical Review Letters, 2008. **100**(1): p. 016602.
14. Chen, J.H., et al., *Intrinsic and extrinsic performance limits of graphene devices on SiO2.* Nature Nanotechnology, 2008. **3**(4): p. 206-209.
15. Saini, A., *EU Graphene Flagship project aims for technological breakthroughs.* Mrs Bulletin, 2014. **39**(5): p. 393-394.
16. Zhu, Y.W., et al., *Graphene and Graphene Oxide: Synthesis, Properties, and Applications.* Advanced Materials, 2010. **22**(35): p. 3906-3924.

17. Yoon, D., Y.W. Son, and H. Cheong, *Negative Thermal Expansion Coefficient of Graphene Measured by Raman Spectroscopy.* Nano Letters, 2011. **11**(8): p. 3227-3231.
18. Zakharchenko, K.V., et al., *Melting of graphene: from two to one dimension.* Journal of Physics-Condensed Matter, 2011. **23**(20): p. 202202.
19. Balandin, A.A., et al., *Superior thermal conductivity of single-layer graphene.* Nano Letters, 2008. **8**(3): p. 902-907.
20. Nair, R.R., et al., *Fine structure constant defines visual transparency of graphene.* Science, 2008. **320**(5881): p. 1308-1308.
21. Zhu, S.E., S.J. Yuan, and G.C.A.M. Janssen, *Optical transmittance of multilayer graphene.* EPL, 2014. **108**(1): p. 17007.
22. Bolotin, K.I., et al., *Ultrahigh electron mobility in suspended graphene.* Solid State Communications, 2008. **146**(9-10): p. 351-355.
23. Dato, A., et al., *Clean and highly ordered graphene synthesized in the gas phase.* Chemical Communications, 2009(40): p. 6095-6097.
24. Bae, S., et al., *Roll-to-roll production of 30-inch graphene films for transparent electrodes.* Nature Nanotechnology, 2010. **5**(8): p. 574-578.
25. Han, S.J., et al., *Graphene radio frequency receiver integrated circuit.* Nature Communications, 2014. **5**.
26. Wang, J.T.W., et al., *Low-Temperature Processed Electron Collection Layers of Graphene/TiO2 Nanocomposites in Thin Film Perovskite Solar Cells.* Nano Letters, 2014. **14**(2): p. 724-730.
27. Wang, W., et al., *Hydrous Ruthenium Oxide Nanoparticles Anchored to Graphene and Carbon Nanotube Hybrid Foam for Supercapacitors.* Scientific Reports, 2014. **4**.
28. Novoselov, K.S., et al., *A roadmap for graphene.* Nature, 2012. **490**(7419): p. 192-200.
29. Cai, J.M., et al., *Atomically precise bottom-up fabrication of graphene nanoribbons.* Nature, 2010. **466**(7305): p. 470-473.
30. Berger, C., et al., *Electronic confinement and coherence in patterned epitaxial graphene.* Science, 2006. **312**(5777): p. 1191-1196.
31. Li, D., et al., *Processable aqueous dispersions of graphene nanosheets.* Nature Nanotechnology, 2008. **3**(2): p. 101-105.
32. Kim, K.S., et al., *Large-scale pattern growth of graphene films for stretchable transparent electrodes.* Nature, 2009. **457**(7230): p. 706-710.
33. Li, X.S., et al., *Large-Area Synthesis of High-Quality and Uniform Graphene Films on Copper Foils.* Science, 2009. **324**(5932): p. 1312-1314.
34. Lee, J.H., et al., *Wafer-Scale Growth of Single-Crystal Monolayer Graphene on Reusable Hydrogen-Terminated Germanium.* Science, 2014. **344**(6181): p. 286-289.
35. Pierson, H.O., *Handbook of chemical vapor deposition*. 2nd ed1999, Norwich, NY: Noyes Publications. xxiv., 482 p.

36. Li, X.S., et al., *Large-Area Graphene Single Crystals Grown by Low-Pressure Chemical Vapor Deposition of Methane on Copper.* Journal of the American Chemical Society, 2011. **133**(9): p. 2816-2819.

37. Choubak, S., et al., *No Graphene Etching in Purified Hydrogen.* Journal of Physical Chemistry Letters, 2013. **4**(7): p. 1100-1103.

38. Zhang, W.H., et al., *First-Principles Thermodynamics of Graphene Growth on Cu Surfaces.* Journal of Physical Chemistry C, 2011. **115**(36): p. 17782-17787.

39. Vlassiouk, I., et al., *Role of Hydrogen in Chemical Vapor Deposition Growth of Large Single-Crystal Graphene.* Acs Nano, 2011. **5**(7): p. 6069-6076.

40. Wofford, J.M., et al., *Graphene Islands on Cu Foils: The Interplay between Shape, Orientation, and Defects.* Nano Letters, 2010. **10**(12): p. 4890-4896.

41. Geng, D.C., et al., *Uniform hexagonal graphene flakes and films grown on liquid copper surface.* Proceedings of the National Academy of Sciences of the United States of America, 2012. **109**(21): p. 7992-7996.

42. Nie, S., et al., *Growth from below: bilayer graphene on copper by chemical vapor deposition.* New Journal of Physics, 2012. **14**: p. 093028.

43. Calado, V.E., et al., *Ballistic transport in graphene grown by chemical vapor deposition.* Applied Physics Letters, 2014. **104**(2): p. 023103.

44. Liang, T., et al., *Variable Charge Reactive Potential for Hydrocarbons to Simulate Organic-Copper Interactions.* Journal of Physical Chemistry A, 2012. **116**(30): p. 7976-7991.

45. Liang, T., et al., *Classical atomistic simulations of surfaces and heterogeneous interfaces with the charge-optimized many body (COMB) potentials.* Materials Science & Engineering R-Reports, 2013. **74**(9): p. 255-279.

46. Daw, M.S. and M.I. Baskes, *Semiempirical, Quantum-Mechanical Calculation of Hydrogen Embrittlement in Metals.* Physical Review Letters, 1983. **50**(17): p. 1285-1288.

47. Daw, M.S. and M.I. Baskes, *Embedded-Atom Method - Derivation and Application to Impurities, Surfaces, and Other Defects in Metals.* Physical Review B, 1984. **29**(12): p. 6443-6453.

48. Brenner, D.W., et al., *A second-generation reactive empirical bond order (REBO) potential energy expression for hydrocarbons.* Journal of Physics-Condensed Matter, 2002. **14**(4): p. 783-802.

49. Stuart, S.J., A.B. Tutein, and J.A. Harrison, *A reactive potential for hydrocarbons with intermolecular interactions.* Journal of Chemical Physics, 2000. **112**(14): p. 6472-6486.

50. Chang, S.W., A.K. Nair, and M.J. Buehler, *Geometry and temperature effects of the interfacial thermal conductance in copper- and nickel-graphene nanocomposites.* Journal of Physics-Condensed Matter, 2012. **24**(24): p. 245301.

51. Reguzzoni, M., et al., *Potential energy surface for graphene on graphene: Ab initio derivation, analytical description, and microscopic interpretation.* Physical Review B, 2012. **86**(24): p. 245434.

Bibliography

52. Zhao, S.J., et al., *Effect of SiO2 substrate on the irradiation-assisted manipulation of supported graphene: a molecular dynamics study.* Nanotechnology, 2012. **23**(28): p. 285703.
53. Chien, S.K., Y.T. Yang, and C.K. Chen, *A molecular dynamics study of the mechanical properties of graphene nanoribbon-embedded gold composites.* Nanoscale, 2011. **3**(10): p. 4307-4313.
54. Xu, Z.P. and M.J. Buehler, *Heat dissipation at a graphene-substrate interface.* Journal of Physics-Condensed Matter, 2012. **24**(47): p. 475305.
55. Guo, Y.F. and W.L. Guo, *Soliton-like thermophoresis of graphene wrinkles.* Nanoscale, 2013. **5**(1): p. 318-323.
56. Liang, T., et al., *Reactive Potentials for Advanced Atomistic Simulations.* Annual Review of Materials Research, Vol 43, 2013. **43**: p. 109-129.
57. Wei, D.S., Y. Song, and F. Wang, *A simple molecular mechanics potential for mu m scale graphene simulations from the adaptive force matching method.* Journal of Chemical Physics, 2011. **134**(18): p. 184704.
58. Devine, B., et al., *Atomistic simulations of copper oxidation and Cu/Cu2O interfaces using charge-optimized many-body potentials.* Physical Review B, 2011. **84**(12): p. 125308.
59. Plimpton, S., *Fast Parallel Algorithms for Short-Range Molecular-Dynamics.* Journal of Computational Physics, 1995. **117**(1): p. 1-19.
60. Nix, F.C. and D. MacNair, *The thermal expansion of pure metals copper, gold, aluminum, nickel, and iron.* Physical Review, 1941. **60**(8): p. 597-605.
61. Jiang, H., et al., *Thermal expansion of single wall carbon nanotubes.* Journal of Engineering Materials and Technology-Transactions of the Asme, 2004. **126**(3): p. 265-270.
62. Pozzo, M., et al., *Thermal Expansion of Supported and Freestanding Graphene: Lattice Constant versus Interatomic Distance.* Physical Review Letters, 2011. **106**(13): p. 135501.
63. Stukowski, A., *Visualization and analysis of atomistic simulation data with OVITO-the Open Visualization Tool.* Modelling and Simulation in Materials Science and Engineering, 2010. **18**(1): p. 015012.
64. Tyson, W.R. and W.A. Miller, *Surface Free-Energies of Solid Metals - Estimation from Liquid Surface-Tension Measurements.* Surface Science, 1977. **62**(1): p. 267-276.
65. Gan, C.K. and D.J. Srolovitz, *First-principles study of graphene edge properties and flake shapes.* Physical Review B, 2010. **81**(12): p. 125445.
66. Cho, J., et al., *Atomic-Scale Investigation of Graphene Grown on Cu Foil and the Effects of Thermal Annealing.* Acs Nano, 2011. **5**(5): p. 3607-3613.
67. Zheng, J.X., et al., *Interfacial Properties of Bilayer and Trilayer Graphene on Metal Substrates.* Scientific Reports, 2013. **3**: p. 2081.
68. Vanin, M., et al., *Graphene on metals: A van der Waals density functional study.* Physical Review B, 2010. **81**(8): p. 081408.

69. Khomyakov, P.A., et al., *First-principles study of the interaction and charge transfer between graphene and metals.* Physical Review B, 2009. **79**(19): p. 195425.
70. Mi, X., et al., *Facet-insensitive graphene growth on copper.* Physical Review B, 2012. **85**(15): p. 155436.
71. Nie, S., et al., *Origin of the mosaicity in graphene grown on Cu(111).* Physical Review B, 2011. **84**(15): p. 155425.
72. Zhang, X.Y., et al., *How the Orientation of Graphene Is Determined during Chemical Vapor Deposition Growth.* Journal of Physical Chemistry Letters, 2012. **3**(19): p. 2822-2827.
73. Murdock, A.T., et al., *Controlling the Orientation, Edge Geometry, and Thickness of Chemical Vapor Deposition Graphene.* Acs Nano, 2013. **7**(2): p. 1351-1359.
74. Olsen, T., et al., *Dispersive and Covalent Interactions between Graphene and Metal Surfaces from the Random Phase Approximation.* Physical Review Letters, 2011. **107**(15): p. 156401.
75. Loginova, E., et al., *Defects of graphene on Ir(111): Rotational domains and ridges.* Physical Review B, 2009. **80**(8): p. 085430.
76. N'Diaye, A.T., et al., *In situ observation of stress relaxation in epitaxial graphene.* New Journal of Physics, 2009. **11**: p. 113056.
77. Chae, S.J., et al., *Synthesis of Large-Area Graphene Layers on Poly-Nickel Substrate by Chemical Vapor Deposition: Wrinkle Formation.* Advanced Materials, 2009. **21**(22): p. 2328-2333.
78. Hattab, H., et al., *Interplay of Wrinkles, Strain, and Lattice Parameter in Graphene on Iridium.* Nano Letters, 2012. **12**(2): p. 678-682.
79. Obraztsov, A.N., et al., *Chemical vapor deposition of thin graphite films of nanometer thickness.* Carbon, 2007. **45**(10): p. 2017-2021.
80. Sun, G.F., et al., *Atomic-scale imaging and manipulation of ridges on epitaxial graphene on 6H-SiC(0001).* Nanotechnology, 2009. **20**(35): p. 355701.
81. Zhang, Y.F., et al., *Defect-like Structures of Graphene on Copper Foils for Strain Relief Investigated by High-Resolution Scanning Tunneling Microscopy.* Acs Nano, 2011. **5**(5): p. 4014-4022.
82. Liu, M.X., et al., *Thinning Segregated Graphene Layers on High Carbon Solubility Substrates of Rhodium Foils by Tuning the Quenching Process.* Acs Nano, 2012. **6**(12): p. 10581-10589.
83. Dean, C.R., et al., *Boron nitride substrates for high-quality graphene electronics.* Nature Nanotechnology, 2010. **5**(10): p. 722-726.
84. Mattevi, C., H. Kim, and M. Chhowalla, *A review of chemical vapour deposition of graphene on copper.* Journal of Materials Chemistry, 2011. **21**(10): p. 3324-3334.
85. Zhang, Y., L.Y. Zhang, and C.W. Zhou, *Review of Chemical Vapor Deposition of Graphene and Related Applications.* Accounts of Chemical Research, 2013. **46**(10): p. 2329-2339.

86. Kobayashi, T., et al., *Production of a 100-m-long high-quality graphene transparent conductive film by roll-to-roll chemical vapor deposition and transfer process.* Applied Physics Letters, 2013. **102**(2): p. 023112.

87. Yan, Z., et al., *Toward the Synthesis of Wafer-Scale Single-Crystal Graphene on Copper Foils.* Acs Nano, 2012. **6**(10): p. 9110-9117.

88. Wu, Y.M.A., et al., *Large Single Crystals of Graphene on Melted Copper Using Chemical Vapor Deposition.* Acs Nano, 2012. **6**(6): p. 5010-5017.

89. Yu, Q.K., et al., *Control and characterization of individual grains and grain boundaries in graphene grown by chemical vapour deposition.* Nature Materials, 2011. **10**(6): p. 443-449.

90. Koepke, J.C., et al., *Atomic-Scale Evidence for Potential Barriers and Strong Carrier Scattering at Graphene Grain Boundaries: A Scanning Tunneling Microscopy Study.* Acs Nano, 2013. **7**(1): p. 75-86.

91. Li, X.S., et al., *Graphene Films with Large Domain Size by a Two-Step Chemical Vapor Deposition Process.* Nano Letters, 2010. **10**(11): p. 4328-4334.

92. Yazyev, O.V. and S.G. Louie, *Electronic transport in polycrystalline graphene.* Nature Materials, 2010. **9**(10): p. 806-809.

93. Petrone, N., et al., *Chemical Vapor Deposition-Derived Graphene with Electrical Performance of Exfoliated Graphene.* Nano Letters, 2012. **12**(6): p. 2751-2756.

94. Gannett, W., et al., *Boron nitride substrates for high mobility chemical vapor deposited graphene.* Applied Physics Letters, 2011. **98**(24): p. 242105.

95. Zomer, P.J., et al., *A transfer technique for high mobility graphene devices on commercially available hexagonal boron nitride.* Applied Physics Letters, 2011. **99**(23): p. 232014.

96. Cheianov, V.V., V. Fal'ko, and B.L. Altshuler, *The focusing of electron flow and a Veselago lens in graphene p-n junctions.* Science, 2007. **315**(5816): p. 1252-1255.

97. Katsnelson, M.I., K.S. Novoselov, and A.K. Geim, *Chiral tunnelling and the Klein paradox in graphene.* Nature Physics, 2006. **2**(9): p. 620-625.

98. Beenakker, C.W.J., *Specular andreev Reflection in graphene.* Physical Review Letters, 2006. **97**(6): p. 067007.

99. Hirayama, Y., et al., *Ballistic Electron-Transport in Macroscopic 4-Terminal Square Structures with High Mobility.* Applied Physics Letters, 1991. **58**(23): p. 2672-2674.

100. Mayorov, A.S., et al., *Micrometer-Scale Ballistic Transport in Encapsulated Graphene at Room Temperature.* Nano Letters, 2011. **11**(6): p. 2396-2399.

101. Vanhouten, H., et al., *Coherent Electron Focusing with Quantum Point Contacts in a Two-Dimensional Electron-Gas.* Physical Review B, 1989. **39**(12): p. 8556-8575.

102. Taychatanapat, T., et al., *Electrically tunable transverse magnetic focusing in graphene.* Nature Physics, 2013. **9**(4): p. 225-229.

103. Ferrari, A.C., et al., *Raman spectrum of graphene and graphene layers.* Physical Review Letters, 2006. **97**(18): p. 187401.

104. Meyer, J.C., et al., *The structure of suspended graphene sheets.* Nature, 2007. **446**(7131): p. 60-63.
105. Haigh, S.J., et al., *Cross-sectional imaging of individual layers and buried interfaces of graphene-based heterostructures and superlattices.* Nature Materials, 2012. **11**(9): p. 764-767.
106. Adam, S., et al., *A self-consistent theory for graphene transport.* Proceedings of the National Academy of Sciences of the United States of America, 2007. **104**(47): p. 18392-18397.
107. Hwang, E.H., S. Adam, and S. Das Sarma, *Carrier transport in two-dimensional graphene layers.* Physical Review Letters, 2007. **98**(18): p. 186806.
108. Kat͡snelʹson, M.I., *Graphene : carbon in two dimensions*. xiv, 351 pages.
109. Avouris, P., *Graphene: Electronic and Photonic Properties and Devices.* Nano Letters, 2010. **10**(11): p. 4285-4294.
110. Min, H. and A.H. MacDonald, *Origin of Universal Optical Conductivity and Optical Stacking Sequence Identification in Multilayer Graphene.* Physical Review Letters, 2009. **103**(6): p. 067402.
111. Kuzmenko, A.B., et al., *Universal optical conductance of graphite.* Physical Review Letters, 2008. **100**(11): p. 117401.
112. Gaskell, P.E., et al., *Counting graphene layers on glass via optical reflection microscopy.* Applied Physics Letters, 2009. **94**(14): p. 143101.
113. Stauber, T., N.M.R. Peres, and A.K. Geim, *Optical conductivity of graphene in the visible region of the spectrum.* Physical Review B, 2008. **78**(8): p. 085432.
114. Kubo, R., *Statistical-Mechanical Theory of Irreversible Processes .1. General Theory and Simple Applications to Magnetic and Conduction Problems.* Journal of the Physical Society of Japan, 1957. **12**(6): p. 570-586.
115. Yuan, S.J., H. De Raedt, and M.I. Katsnelson, *Modeling electronic structure and transport properties of graphene with resonant scattering centers.* Physical Review B, 2010. **82**(11): p. 115448.
116. Yuan, S.J., et al., *Optical conductivity of disordered graphene beyond the Dirac cone approximation.* Physical Review B, 2011. **84**(19): p. 195418.
117. Yuan, S.J., R. Roldan, and M.I. Katsnelson, *Excitation spectrum and high-energy plasmons in single-layer and multilayer graphene.* Physical Review B, 2011. **84**(3): p. 035439.
118. Wang, Y.Y., et al., *Interference enhancement of Raman signal of graphene.* Applied Physics Letters, 2008. **92**(4): p. 043121.
119. Lin, Y.M., et al., *100-GHz Transistors from Wafer-Scale Epitaxial Graphene.* Science, 2010. **327**(5966): p. 662-662.
120. Mueller, T., F.N.A. Xia, and P. Avouris, *Graphene photodetectors for high-speed optical communications.* Nature Photonics, 2010. **4**(5): p. 297-301.
121. Lee, Y., et al., *Wafer-Scale Synthesis and Transfer of Graphene Films.* Nano Letters, 2010. **10**(2): p. 490-493.

122. Barlian, A.A., et al., *Review: Semiconductor Piezoresistance for Microsystems.* Proceedings of the Ieee, 2009. **97**(3): p. 513-552.
123. Bae, S.H., et al., *Graphene-based transparent strain sensor.* Carbon, 2013. **51**: p. 236-242.
124. Wang, Y., et al., *Super-Elastic Graphene Ripples for Flexible Strain Sensors.* Acs Nano, 2011. **5**(5): p. 3645-3650.
125. Huang, M.Y., et al., *Electronic-Mechanical Coupling in Graphene from in situ Nanoindentation Experiments and Multiscale Atomistic Simulations.* Nano Letters, 2011. **11**(3): p. 1241-1246.
126. Zhu, S.E., et al., *Graphene-Based Bimorph Microactuators.* Nano Letters, 2011. **11**(3): p. 977-981.
127. Neugebauer, C.A., *Structure and properties of thin films*1959, New York,: Wiley. xiv, 561 p.
128. Creemer, J.F., et al., *A MEMS Reactor for Atomic-Scale Microscopy of Nanomaterials Under Industrially Relevant Conditions.* Journal of Microelectromechanical Systems, 2010. **19**(2): p. 254-264.
129. Allen, M.G., et al., *Microfabricated Structures for the Insitu Measurement of Residual-Stress, Youngs Modulus, and Ultimate Strain of Thin-Films.* Applied Physics Letters, 1987. **51**(4): p. 241-243.
130. MaierSchneider, D., J. Maibach, and E. Obermeier, *A new analytical solution for the load-deflection of square membranes.* Journal of Microelectromechanical Systems, 1995. **4**(4): p. 238-241.
131. Gavan, K.B., et al., *Impact of fabrication technology on flexural resonances of silicon nitride cantilevers.* Microelectronic Engineering, 2009. **86**(4-6): p. 1216-1218.
132. Anker, J.N., et al., *Biosensing with plasmonic nanosensors.* Nature Materials, 2008. **7**(6): p. 442-453.
133. Ritchie, R.H., *Plasma Losses by Fast Electrons in Thin Films.* Physical Review, 1957. **106**(5): p. 874-881.
134. Grigorenko, A.N., M. Polini, and K.S. Novoselov, *Graphene plasmonics.* Nature Photonics, 2012. **6**(11): p. 749-758.
135. Principi, A., et al., *Intrinsic lifetime of Dirac plasmons in graphene.* Physical Review B, 2013. **88**(19): p. 195405.
136. Principi, A., et al., *Impact of disorder on Dirac plasmon losses.* Physical Review B, 2013. **88**(12).
137. Fei, Z., et al., *Gate-tuning of graphene plasmons revealed by infrared nano-imaging.* Nature, 2012. **487**(7405): p. 82-85.
138. Chen, J.N., et al., *Strong Plasmon Reflection at Nanometer-Size Gaps in Monolayer Graphene on SiC.* Nano Letters, 2013. **13**(12): p. 6210-6215.
139. Chen, J.N., et al., *Optical nano-imaging of gate-tunable graphene plasmons.* Nature, 2012. **487**(7405): p. 77-81.

140. Fei, Z., et al., *Infrared Nanoscopy of Dirac Plasmons at the Graphene-SiO2 Interface.* Nano Letters, 2011. **11**(11): p. 4701-4705.
141. Atwater, H.A., *The promise of plasmonics.* Scientific American, 2007. **296**(4): p. 56-63.
142. Dai, S., et al., *Tunable Phonon Polaritons in Atomically Thin van der Waals Crystals of Boron Nitride.* Science, 2014. **343**(6175): p. 1125-1129.
143. Huth, F., et al., *Infrared-spectroscopic nanoimaging with a thermal source.* Nature Materials, 2011. **10**(5): p. 352-356.
144. Yan, H.G., et al., *Infrared Spectroscopy of Wafer-Scale Graphene.* Acs Nano, 2011. **5**(12): p. 9854-9860.
145. Vakil, A. and N. Engheta, *Transformation Optics Using Graphene.* Science, 2011. **332**(6035): p. 1291-1294.
146. Nikitin, A.Y., et al., *Edge and waveguide terahertz surface plasmon modes in graphene microribbons.* Physical Review B, 2011. **84**(16): p. 161407.
147. Volkov, V.A. and S.A. Mikhailov, *Edge Magnetoplasmons - Low-Frequency, Weakly Decaying Excitations in Inhomogeneous Two-Dimensional Electron-Systems.* Zhurnal Eksperimentalnoi I Teoreticheskoi Fiziki, 1988. **94**(8): p. 217-241.
148. Schmidt, F.P., et al., *Universal dispersion of surface plasmons in flat nanostructures.* Nature Communications, 2014. **5**: p. 3604.
149. Geim, A.K. and P. Kim, *Carbon wonderland.* Scientific American, 2008. **298**(4): p. 90-97.

Samenvatting

Inleiding

Experimenteel werk aan grafeen is begonnen met de baanbrekende publicatie van prof Novoselov en Geim in 2004 [3]. In die publicatie zijn de eigenschappen van grafeen aangeprezen als: "Grafeen zou het best mogelijke metaal kunnen worden voor metallische transistor toepassingen..., maar niet-transistor toepassingen van dit atomair dunne materiaal zouden uiteindelijk het meest spannend kunnen blijken." De toekenning van de Nobelprijs in 2010 heeft de wetenschappelijke gemeenschap verder geïnspireerd en een grote investering van de Europese Unie tot stand kunnen brengen (10 jaar onderzoeksinitiatief: "Europese Grafeen Flagship"). Deze snelle ontwikkeling zorgt ervoor dat de samenleving droomt over de praktische toekomstige toepassingen van grafeen.

De status van een opkomende technologie van zijn ontdekking tot consumentenproducten kunnen worden geplaatst volgens de door Gartner Reseach (afb. 8.1) voorgestelde technologie levenscyclus curve. Een succesvolle technologie ervaart meestal de volgende vijf belangrijke fasen: Technology trigger, piek van opgeblazen verwachtingen, dal van de desillusie, helling van verlichting, en plateau van productiviteit. Met deze kromme is het mogelijk om een technologie hype van valorisatie te onderscheiden. Het baanbrekende experiment in 2004 kan worden herkend als het startpunt van de grafeen-technologie. De toekenning van de Nobelprijs voor de Natuurkunde in 2010 en de toekenning van 10 jaar project "Europese Grafeen Flasghip" zou zeker worden gemarkeerd in de piek van de opgeblazen verwachtingen voor grafen-technologie. Het aantal start-up bedrijven groeit explosief van minder dan 5 in 2010 tot meer dan 50 in 2014. Hoewel het onderwerp van grafeen voortdurend de samenleving in spanning heeft gehouden, staat de feitelijke ontwikkeling nog in de kinderschoenen. Het merendeel van de bedrijven is momenteel gericht zijn op het leveren van grondstoffen of productiemachines. De belangrijkste drijvende krachten zij tot dusver afkomstig uit academisch onderzoek en de R&D sector in de industrie. Voor grafeen ontbreekt vooralsnog een killer application.

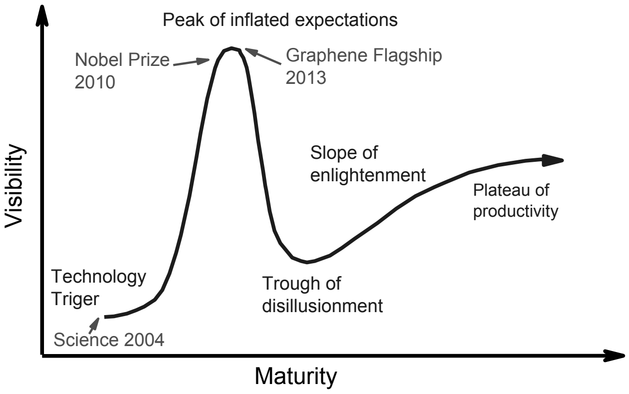

Figuur 8.1: De levenscyclus van opkomende technologieën. Vijf belangrijke fasen worden aangegeven op de horizontale y-as, Technology trigger, piek van opgeblazen verwachtingen, dal van de desillusie, helling van verlichting, en plateau van productiviteit. (Afbeelding is herleid van de Hype Cycle van Gartner Research)

Welke bijdrage levert dit proefschrift aan de ontwikkeling van een grafeen-technologie

In dit proefschrift heb ik aangetoond dat de kwaliteit van synthetische grafeen zo hoog als mechanisch geëxfolieerd grafeen kan zijn mits we de rimpels weg kunnen krijgen. Alle defecten, onzuiverheden en korrelgrenzen zal verstrooiing veroorzaken, wat ballistisch transport in de weg zit. Het experiment beschreven in hoofdstuk 4 was het eerste om ballistische vervoer in synthetische grafeen aan te tonen, en het zal de weg voor de massale productie van hoge kwaliteit monolaag grafeen effenen. In 2008 was het maken van een monolaag grafeen moeilijk en het gerangschikt als de duurste materiaal in de wereld. Een stuk van mechanisch geëxfolieerde monolaag grafeen met een grootte kleiner dan de diameter van een menselijke haar zal meer kosten dan \$ 1000 uit Grafeen Research Ltd in Manchester [149]. Op dit moment (2014), Monolayer grafeen, bestaande uit enkele kristallen met grootte tot millimeter in diameter, zijn al routinematig wereldwijd geproduceerd, en de prijs per cm^2 monster is gedaald tot minder dan \$ 200.

In hoofdstuk 5 van dit proefschrift werd een parameterloze vergelijking geleverd om het aantal grafeen lagen te berekenen door het meten van de transmissie van grafeen films. De zoektocht naar nieuwe transparante elektrode materialen met goede stabiliteit, hoge transparantie en uitstekende geleiding wordt gestuurd door de vereiste afweging tussen doorzichtigheid en geleidbaarheid: Metalen zijn sterk geleidend maar niet transparant; kunststoffen zijn vrij transparant maar niet geleidend. Grafeen is een doorzichtig en geleidend materiaal. Echter, kan de geleidbaarheid van monolaag grafeen niet voldoende voor het vervaardigen van een sterk geleidende elektrode. Het dilemma is dat de transmissie van een grafeen film afneemt als het aantal lagen toeneemt. Het is daarom van groot belang om een snelle en betrouwbare methode om het aantal lagen in de fabricage en meting van multilayer grafeen te bepalen. Een eenvoudige relatie die bepaalt hoeveel grafeen lagen aan de transmissie eisen voldoen en tegelijkertijd een goede geleiding levert is een waardevol instrument.

Verder heb ik de integratie van grafeen in siliciumchips gedemonstreerd, wat een druksensor apparaten mogelijk maakt dat op waferschaal geproduceerd kan worden. Een gevoeligheid van ~8.5 mV/bar werd verkregen met een standaardafwijking van minder dan 15 mbar bij 700 mbar volledige schaal. Deze integratie van grafeenapparaten op chipschaal is een essentieel proces om de huidige halfgeleidertechnologie en de toekomstige toepassingen van hoge kwaliteit grafeenfilms te koppelen. De verdere ontwikkeling van wafer schaal automatisering proces van overdracht staat op de routebeschrijving naar de valorisatie van grafeen.

In hoofdstuk 7 van dit proefschrift heb ik de mogelijke toepassing van grafeen voor opto-elektronica apparaten getoond. De snelheid van opto-elektronica zal de huidige transistoren beter presteren dan vooral in hoog-volume informatie zenden op chip schaal.

Hoewel er nog veel technische problemen wachten te worden opgelost en de levering van hoge kwaliteit grafeen gebaseerde producten in grote hoeveelheden nog steeds een belangrijke kwestie is, heeft grafeen onderzoek desalniettemin een enorme vooruitgang geboekt.

Op een termijn van 10-20 jaar, geloof ik dat de prijs van grootschalige monolaag grafeen zal dalen tot onder \$ 1 / cm^2 vergelijkbaar met de prijs van de gate-oxide, dat grafeen in staat zal stellen om potentiële markten, zoals opto-elektronische berekeningen, flexibel in te voeren sensoren en draagbare apparaten, etc. Er is een mooie toekomst voor grafeen technologie.

Curriculum Vitae

Shou-En Zhu

2011-2014 **Doctor of Philosophy, Micro and Nano Engineering**, Delft University of Technology (TU Delft), the Netherlands (awaiting thesis defence)
• Thesis title: Chemical vapor deposition of graphene: a route to device integration.
Visiting Scholar at UC San Diego. (2014.03-2014.07).
Guest Researcher at ETH Zurich. (2012.09-2012.10).
Guest Researcher at Leiden University. (2011.01-2011.04).

2012-now **Founder of Graphene Master,** one of the innovative nanotechnology companies (awarded by NanoLabNL Foundation) in the Netherlands.

Education

2008-2010 **Master of Engineering, Materials Science and Engineering**, Jilin University, China
• Thesis title: Large-scale synthesis and transfer of graphene.
Exchange at Sungkyunkwan University. (2009.08-2010.12)

2004-2008 **Bachelor of Engineering, Materials Science and Engineering**, Jilin University, Jilin, China
• GPA: 88/100 (top 5% of grade)
Exchange at Feng Chia University. (2007.09-2008.01).

2001-2004 **High school in science,** Fuzhou No.3 High School
• Merit Student of the city

Awards, Distinctions and Fellowships

1. NanoLabNL Voucher (7,500 EUR) from NanoLabNL Foundation. (2014)
2. Energy Initiative Award (10,000 EUR) at TU Delft. (2014)
3. Onassis Travel Grant (~1,000 EUR) from "Alexander S. Onassis Public Benefit Foundation". (2013)
4. Chinese Government Award (6,000 USD) for Outstanding Self-Financed Students Abroad. (2012)
5. IDEA League Grant (3,000 EUR). (2012)
6. Young Wild Idea Prize (10,000 EUR) at Delft Center of Materials. (2011)
7. The First Prize Scholarship. (2005, 2006, 2008, 2009, 2010)

List of Publications

Peer review journal:

9. Peter Klaver, Shou-En Zhu, Marcel Sluiter, Guido Janssen, Molecular dynamics simulation of graphene on Cu (100) and (111) surfaces. Carbon 82, 538-547 (2014).
8. Shou-En Zhu, Shengjun Yuan, G.C.A.M. Janssen, Optical transmittance of multilayer graphene. EPL (Europhysics Letters) 108, 17007 (2014).
7. Victor Calado*, Shou-En Zhu*, Srijit Goswami, Qiang Xu, Kenji Watanabe, Takashi Taniguchi, G.C.A.M. Janssen, Lieven Vandersypen, Ballistic transport in graphene grown by chemical vapor deposition. Applied Physics Letters 104, 023103 (2014) (Cover Feature) (* these authors contributed equally).
6. Shou-En Zhu, Murali Krishna Ghatkesar, Chao Zhang, and G. C. A. M. Janssen. Graphene Based Piezoresistive Pressure Sensor. Applied Physics Letters. 102, 161904 (2013).
5. Zhiteng Wang*, Shou-En Zhu*, Yu Chen, Man Wu, Chujun Zhao, Han Zhang, G.C.A.M. Janssen, Shuangchun Wen. Multilayer graphene for Q-switched mode-locking operation in an erbium-doped fiber laser. Optics Communications 300, 17-21 (2013). (* these authors contributed equally)
4. Young In Jhon, Shou-En Zhu, Jong-Hyun Ahn, Myung S. Jhon, The Mechanical Responses of Tilted and Non-tilted Grain Boundaries in Graphene. Carbon, 50, 3708-3716 (2012)
3. Shou-En Zhu, Roxana Shabani, Jonghyun Rho, Youngsoo Kim, Byung Hee Hong, Jong-Hyun Ahn, and Hyoung J. Cho, Graphene-Based Bimorph Microactuators. Nano Letters, 11, 977-981 (2011). (Nature Asia Materials featured highlight | Microactuators: Graphene on dragonfly wings)
2. W. Gao, S. E. Zhu, M. Zhao, Methylthiolate adsorbed on as-rich GaAs (001) surface. Journal of Materials Science 46, 1021-1026 (2011).
1. Youngbin Lee, Sukang Bae, Houk Jang, Sukjae Jang, Shou-En Zhu, Sung Hyun Sim, Young Il Song, Byung Hee Hong, and Jong-Hyun Ahn, Wafer Scale Synthesis and Transfer of graphene films. Nano Letters, 10, 490-493 (2010). (top 10 read in 2010)

Patents:

1. Shou-En Zhu et al. Graphene Synthesis.
2. Shou-En Zhu et al. Graphene transfer.

Conferences:

1. Shou-En Zhu, Peter Klaver, Marcel Sluiter, G.C.A.M. Janssen, "Graphene Grown by Chemical Vapor Deposition", Gordon Research Seminar, Graphitic Carbon Materials. June 14-15, 2014, Bates College, Lewiston, USA. (Oral Presentation)
2. Shou-En Zhu, “Single crystal graphene for water purification”, All Energy Day, March 14, 2014, Den Haag, the Netherlands. (Oral Presentation)
3. Shou-En Zhu, "CVD Graphene towards Future Applications", Dutch Graphene Day, October 25, 2013, Eindhoven, the Netherlands. (Oral Presentation)
4. Shou-En Zhu, Victor E. Calado, Lieven M.K. Vandersypen, G.C.A.M. Janssen, "Ballistic quantum transport in CVD graphene", Dutch Graphene Day, May 3, 2013, Utrecht, the Netherlands. (Oral Presentation)
5. Shou-En Zhu, Victor E. Calado, Lieven M.K. Vandersypen, G.C.A.M. Janssen, “Controllable synthesis of large monolayer and multilayer graphene crystals”, Graphene 2013, April 23-26 Bilbao, Spain. (Oral Presentation)
6. Shou-En Zhu, “Go for CVD graphene”, Graphene Flagship at TU Delft, March 13, Delft, the Netherlands. (Oral Presentation)
7. Shou-En Zhu, Victor E. Calado, Chao Zhang, G.C.A.M. Janssen, "Graphene nanomechanical piezoresistive sensor", Graphene 2012, April 10-13, Brussels, Belgium.
8. Shou-En Zhu, Victor E. Calado, Chao Zhang, G.C.A.M. Janssen, "Graphene based Piezoresistive Cantilever." Graphene Week 2012, June 4-8, Delft, the Netherlands.
9. Shou-En Zhu, Klára Uhlířová, Victor E. Calado, C. Kwakernaak, W.G. Sloof, L.M.K. Vandersypen, J. Aarts, G.C.A.M. Janssen, "Characterization of graphene films synthesized on large grain copper foil", FOM Physics@Veldhoven 2012, Jan 17-18, Veldhoven, the Netherlands.
10. Shou-En Zhu, Ho Jin Kim, Sung Hyun Sim, Hyeongkeun Kim, Byung Hee Hong, Jong-Hyun Ahn, “Transparent and Flexible Heat Spreader of Graphene Films”, Recent Advances in Graphene and Related Materials (Engineering Conferences International), August 1-6, 2010, Singapore.
11. Shou-En Zhu, Guangyu Li, Jong-Hyun Ahn, Hyoung J Cho, “Large-scale Synthesis of Graphene Films and Their Application for a Novel Thermal Actuator”, International Conference on Mechanical Properties of Materials (ICMPM), May 24-28, 2010, Hangzhou, P.R. China. (Oral Presentation)

Other academic activities:

I am serving as an independent reviewer for scientific journal: “ACS Applied Materials and Interfaces”, “Nanoscale”, “Applied Physics Letters”, “IEEE Sensor Journal”, “IEEE Electron Device Letters” and “AIP Advances”.

Acknowledgement

Apart from the acknowledgement to my coworkers at the end of each chapter, I would like to express my deepest thanks to the following people for their support during my PhD career.

First, I want to thank to all the members of my doctoral committee for reviewing my thesis. I would like to thank my promoter Prof. Guido Janssen for offering me this position. I cannot thank you enough for your time, patient and support. Prof. Dirk Gravesteijn, I still remember that we took the photo in front of my homemade furnace. You are the first visitor of my furnace. Prof. Peter Steeneken, thank you for recalculating the equation in my thesis. Prof. Jurriaan Schmitz, I didn't feel surprised about the misery of graphene sample I have sent and a few months down of the Helium ion microscope. I felt so happy that I decided to build my own setup. Prof. Ronald Dekker, I learned a lot from your website and the flexible electronics. Hope that I can have some collaboration with you in the future. Prof. Henny Zandbergen, thank you very much for the support of TEM work, and I still believe that I will have at least one publication with you in the future. Dr. Marcel Sluiter, I always heard that you are a very knowledgeable scientist, and I can thoroughly confirm it again though our collaboration.

I appreciate Dr. Jong-Hyun Ahn and Dr. Byung-Hee Hong. Your ambition and exploration in your early research career inspired me to think about the future. I also want to congratulate your great achievement! Youngbin Lee, Houk Jang, SeoungKi Lee, JongHyun Rho, KyungYea Park, Sukjae Jang, Chao Yan, WonHo Lee, JeeHoon Kim, SangHoon Bae, I can still remember the moment that all of us finished the experiment at midnight on every Friday and had fried chicken and beer. I am indebted to all of you.

Prof. Lieven Vandersypen, thank you very much for allowing me to access your lab and having regular group meeting with you. Victor Calado, thank you very much for the great work of ballistic transport measurement in CVD graphene. I appreciated a lot of your effort and time with me (Including the Dutch translation of the proposition and the summary of this thesis). Stijn Goossens, thank you very much for your enthusiasm of bringing me to different thoughts and projects. Kavli Nanolab staff: Frank Dirne, Paul Alkemade, Charles de Boer, Roel Matter, Anja van Langen-Suurling, Arnold van Run, Marc Zuiddam, Gaurav Nanda, Margit de Kok, thank you all for all the support in the cleanroom fabrication.

Prof. Joost Frenken, Prof. Aarts Jan, Klára Uhlířová, Guicai Dong, Zunfeng liu, Qian Li, Dapeng Ding, Dirk van Baarle, thank you very much for hosting me during my stay at Leiden University.

Prof. Dimitri Basov, Prof. Michael Fogler, Zhe Fei, Siyuan Dai, Mengkun Liu, Michael Goldflam, Alex Swinton McLeod, Yinming Shao, Ted stinson, Kirk Post, Aaron Sternbach, Guangxin Ni, thank you for helping me during my stay at UC San Diego. Prof. Yongfu Zhu, Zhichao Xie, I want to express my gratitude to you for your support.

Dr. Hyung Gyu Park, Jakob Buchheim, Kemal Celebi, Mengmeng Deng, Ning Yang, Jongwon Choi, Seul Ki Youn, Eunjeong Gross, thank you all for hosting me during my stay at ETH Zurich.

Henk, Tamara, Marek, Choi, Maviz, Rob, Gim, Jane, Hans, Daniel, Joel, Jeroen, Fengju, Stefan, Pan, Koen, Holsan, John, Jenny, Carolien, Ifi, Leo, Lydia, and little children: Eric, Luck, Joshua, Timothy, Victoria, I very enjoy very much to spend time with all of you in Delft.

Kun Zuo, Sau Koh, thank you for having dinner with me every one or two weeks, and all those inspiring discussions.

PME staff members: Prof. Urs Staufer, Fred van Keulen, Rob Munning Schmidt, Just Herder, Marcel Tichem, Merlijn van Spengen, Murali Ghatkesar, Mattijs Langelaar, Hans Goosen, Luigi Sasso, Jan Neve, Gerald Wissse, Paolo Tiso, Ivan Buijnsters, Support staff: Gaby, Corinne, Marli, Marianne, Birgit, Eveline, Lab staff: Rob, Harry, Jos, Patrick, MNE group member: Ivan, Alexandre, Yujian, An, Eda, Hugo, Hans, Federico, Girish, Tjitte-Jelte, Jaap, Adnan, Yueting, Alkisti, Enrique, and PhD roommate Banafsheh, Rob Dedden, Selman, Michael, Umut, Maarten, Rob Eling, Long Wu, and Chinese colleague: Qi Wang, Ruijun, thank you very much for helping me in PME at TU Delft and your kind support.

MSE staff members: Prof. Barend Thijsse, Pro. Joris Dik, Wim Sloof, Yulia, Fengwei, Deniz, Georgina, Lie Zhao, Guiming Song, Yongxiang Yang, Neha, Xi Zhang, Fidel, Kelvin, Sebastian, Amarante, Kees, Hans, Lambert, Ruud, Niek, thank you for helping me in MSE at TU Delft and your kind support. Peter Klaver, thank you for the simulation work.

Robin, Sebastiaan, Taco, Islob, thank you for your creative thoughts, and I would like to congratulate your cum laude for your bachelor project. Robin, you did once more a good job for your master cum laude.

My roommates: Jiaqi, Jing Wang, Lu Wang, Dashu, thank you very much for all your help in these years.

Freddy, Sukhjinder, Remko, Patrick, Bonnie, Nico, Antoine, Leen, I would like to thank your efforts during my business development.

Rob Speekenbrink, Liesbeth Mantel, Sylvia Walsarie Wolff, Antoinette Wijffels, Toine Andernach, Jet van Paassen, Jonathan Talbott, Kim van der Linden, I would like to thank you all for guiding me through my most important public talk in TEDxDelft. Anping Cao, Jos van Driel thank you for the help of experiment preparation.

Young Wild Idea committee chairman: Niels van Dijk, secretary: Shanta Visser; Delft Energy Initiative Fund chairman: Paulien Herder, secretary: Eveline Zeegers, Stef Smits; thank you all for approval and support. Without this extra financial support, I couldn’t see any hope during my PhD career. Christina and Roche, thank you for the design work, I appreciate your effort a lot.

I will leave some space here, if I forgot to thank anyone, I will handwrite your name:

Finally, I would thank my family members: my grandfathers, my grandmothers, my uncles, my aunts, my parents, my wife, and my brother and sister-in-law and all those people that I do not name here. Without any of you, I couldn’t imagine how I can finish my PhD research in the Netherlands. I would express my deepest thanks especially to my wife and my guilty of being far away from you.